

## Chapter 4

# Effects of Plate Bending and Fault Strength at Subduction Zones on Plate Dynamics

Published in *Journal of Geophysical Research* by C. P. Conrad and B. H. Hager, *104*, 17551-17571, 1999. Copyright by the American Geophysical Union.

**Abstract.** For subduction to occur, plates must bend and slide past overriding plates along fault zones. Because the lithosphere is strong, significant energy is required for this deformation to occur, energy that could otherwise be spent deforming the mantle. We have developed a finite element representation of a subduction zone in which we parameterize the bending plate and the fault zone using a viscous rheology. By increasing the effective viscosity of either the plate or the fault zone, we can increase the rates of energy dissipation within these regions and thus decrease the velocity of a plate driven by a given slab buoyancy. We have developed a simple physical theory that predicts this slowing by estimating a convecting cell's total energy balance while taking into account the energy required by inelastic deformation of the bending slab and shearing of the fault zone. The energy required to bend the slab is proportional to the slab's viscosity and to the cube of the ratio of its thickness to its radius of curvature. The distribution of dissipation among the mantle, lithosphere, and fault zone causes the speed of a plate to depend on its horizontal length scale. Using the

observation that Earth’s plate velocities are not correlated to plate size, we can constrain the lithosphere viscosity to be between 50 and 200 times the mantle viscosity, with higher values required if the fault zone can support shear tractions  $\gtrsim 50$  MPa over 300 km. These subduction zone strengths imply that the mantle, fault zone, and lithosphere dissipate about 30%, 10%, and 60% of a descending slab’s potential energy release if the slab is 100 km thick. The lithospheric component is highly dependent on slab thickness; it is smaller for thin plates but may be large enough to prevent bending in slabs that can grow thicker than 100 km. Subduction zone strength should be more stable than mantle viscosity to changes in mantle temperature, so the controlling influence of subduction zones could serve to stabilize plate velocities over time as the Earth cools. Because the “details” of convergent plate boundaries are so important to the dynamics of plate motion, numerical models of mantle flow should treat subduction zones in a realistic way.

## 4.1 Introduction

The tectonic motions of Earth’s plates are thought to represent the upper boundary layer of convection in the mantle. This boundary layer founders in a few localized downwellings known as subduction zones in which one plate dives beneath another into the mantle’s interior. It is thought that the negative buoyancy associated with cold, dense slabs drives plate motions by pulling on the surface plates to which these slabs are attached [e.g., *Chapple and Tullis*, 1977; *Forsyth and Uyeda*, 1975; *Hager and O’Connell*, 1981; *Lithgow-Bertelloni and Richards*, 1995]. The cold temperatures of the boundary layer make it not only denser but stiffer than the mantle, a fact that has important implications for convection in the mantle. For example, several authors [e.g., *Bunge and Richards*, 1996; *Davies*, 1988; *Gurnis and Zhong*, 1991] have noted that the long-wavelength structure of mantle flow is at least partly controlled by the existence of strong surface plates.

Convection of a fluid with a strong upper boundary layer has been studied by several authors. In fluids with temperature-dependent viscosity, *Jaupart and Parsons*

[1985] found that two length scales of instability are possible. For large viscosity contrasts between the boundary layer and the underlying fluid, deformation of the entire upper boundary layer becomes sufficiently difficult that it cannot participate in convection. In this case, short-wavelength instabilities develop below a “rigid lid.” For intermediate viscosity contrasts the upper boundary layer can participate in the convective circulation, but its strength produces wavelengths that are longer than would be expected for an isoviscous fluid. *Solomatov* [1995] describes this convective regime as a transitional one between the isoviscous and the rigid lid regimes, distinguished by the significant resistance to flow offered by the cold boundary layer. This resistance can rival that due to shearing of the interior, meaning that the strong upper boundary layer is important in determining convective behavior.

Because the boundary layer is so important, the details of how it deforms should be important as well. In standard isoviscous boundary layer theory, first used to describe mantle convection by *Turcotte and Oxburgh* [1967], downwellings are symmetrical and result in horizontal shortening of the material at the surface above them. Thus, some material at the surface stagnates above the descending plume while cold material from either side flows beneath it. The downwellings associated with plate-scale convection in the mantle do not behave in this manner. Instead, in a subduction zone, one plate bends and descends into the mantle beneath another, even if both plates are composed of oceanic lithosphere. This one-sided downwelling allows more of the thermal buoyancy of the boundary layer to participate in driving plate motions than is achieved in the rigid lid or isoviscous styles of convection. It is not clear, however, if this increased buoyancy is offset by the increased resistance to deformation imposed by the subducting plate’s strength.

There is evidence that resistance to convection is created by the subduction zone. First, the seismicity of Wadati-Benioff zones illuminates the location of the slab [e.g., *Isacks and Barazangi*, 1977; *Giardini and Woodhouse*, 1984]. The fact that energy is released by earthquakes within the slab indicates that the descending lithosphere must generate at least some resistance to mantle convection. In addition, the focal mechanisms associated with this seismicity seem, in some cases, to indicate a stress pattern

in the slab characteristic of bending as the slab begins to descend, and unbending as it straightens out and continues into the mantle [e.g., *Bevis, 1986; Hasegawa et al., 1994; Kawakatsu, 1986*]. The dissipation of energy within the slab as it both bends and unbends indicates that at least some of the bending deformation is inelastic and is undone by more inelastic deformation in an unbending process [e.g., *Chapple and Forsyth, 1979*].

The presence of inelastic deformation in the slab is indicative of the type of rheology that controls the slab's behavior. The topography and gravity of trenches associated with subduction can be explained by theoretical models of the bending of an elastic plate  $\sim 30$  km thick [e.g., *Hanks, 1971; Watts and Talwani, 1974*]. If the radius of curvature of a bending plate is  $R = 200$  km [e.g., *Bevis, 1986*], its Young's modulus is  $E = 70$  GPa [e.g., *Turcotte and Schubert, 1982, p. 106*], and its Poisson's ratio is  $\nu = 0.25$ , we estimate, following *Turcotte and Schubert [1982, p. 114]*, that the maximum bending stresses in the plate must be of order 6000 MPa. This figure is about an order of magnitude larger than the maximum strength of oceanic lithosphere [e.g., *Kohlstedt et al., 1995*], so at most only 10% of elastic bending stresses can be supported. The remaining stress must be relaxed by an inelastic deformation mechanism. For an elastic-plastic or elastic-brittle rheology, elastic stresses greater than the maximum yield stress are relieved by fracturing of the rock [e.g., *Turcotte and Schubert, 1982, pp. 341-345*]. This type of rheology can produce the seismicity distributions of the Benioff zones, which are, perhaps coincidentally, also  $\sim 30$  km wide [e.g., *Hasegawa et al., 1994; Jarrard, 1986; Kawakatsu, 1986*]. In a viscoelastic rheology, viscous strains relax large elastic stresses [e.g., *Turcotte and Schubert, 1982, pp. 337-340*]. We expect the lithosphere to exhibit some viscous properties because it is partly composed of cold mantle material, and the mantle certainly behaves as a highly temperature-dependent viscous fluid. In fact, some authors have shown that trench topography can be explained by the loading of a viscous plate [e.g., *De Bremaecker, 1977*], by viscous stresses associated with bending [e.g., *Melosh and Raefsky, 1980*], or by viscous coupling of the surface to the negative buoyancy of the slab [e.g., *Sleep, 1975; Zhong and Gurnis, 1994*].

The oceanic lithosphere probably experiences all of the above mentioned deformation mechanisms at various stages during subduction, making a full description of the applicable constitutive relation extraordinarily complicated. We recognize, however, that all of the deformation mechanisms, with the exception of elastic bending, dissipate energy and thus retard the flow of the lithosphere into the mantle. In what follows, we estimate the energy dissipated by a deforming slab assuming viscous flow and compare it to the energy dissipated by flow in the underlying mantle. In doing so, we are able to determine how plate velocities depend on the material strength of the subducting lithosphere, which we express as the lithosphere’s “effective” viscosity. Because we are simply performing an energy balance, this parameter can be thought of as allowing viscous flow to dissipate the same energy that would be dissipated if all of the complicated deformation mechanisms were included. Because the effective lithosphere viscosity results from some combination of many deformation mechanisms whose relative and absolute strengths are not known, we treat the effective viscosity as a variable upon which plate velocity depends. Using Earth’s observed distribution of plate velocities, we hope to constrain the value of this parameter and, as a result, the importance of subduction to the large-scale convective structure of Earth.

## 4.2 Viscous Dissipation

One way to determine the relative importance of the slab, fault zone, and mantle is to compare the energy dissipated in deforming each of these regions. To do this, we start with conservation of momentum for a continuous medium:

$$\rho \frac{\partial u_i}{\partial t} + \rho u_j \frac{\partial u_i}{\partial x_j} = f_i + \frac{\partial \sigma_{ij}}{\partial x_j} \quad (4.1)$$

where  $f_i$  is a body force,  $\sigma_{ij}$  is the stress,  $\rho$  is density,  $t$  is time, and  $u_i$  and  $x_i$  are the velocity and distance components. To obtain an expression for energy, we multiply (4.1) by  $u_i$  and integrate over a volume  $V$ . After some manipulation [e.g.,

Chandrasekhar, 1961, pp. 12-14], we obtain

$$\begin{aligned} & \frac{1}{2} \int_V \rho \frac{\partial}{\partial t} u_i^2 dV + \frac{1}{2} \int_S \rho u_i^2 u_j dS_j \\ &= \int_S u_i \sigma_{ij} dS_j - \int_V \sigma_{ij} \frac{\partial u_i}{\partial x_j} dV + \int_V u_i f_i dV \end{aligned} \quad (4.2)$$

where  $S$  is the surface of the volume  $V$ . These five terms express the energy balance for viscous flow, and only the last two contribute significantly for the mantle. The left-hand side gives the rate at which the fluid's kinetic energy changes with time and is negligible if the Reynolds number is low, as it is for the mantle. The first term on the right-hand side is the rate at which stresses do work on the boundary of  $V$ . If  $V$  is the volume of a closed convecting cell with free-slip boundary conditions, this term is zero.

The middle term on the right-hand side of (4.2) represents the rate at which work is done on the medium by the deformation. It is useful to decompose the total stress  $\sigma_{ij}$  into its pressure  $p$  and deviatoric  $\tau_{ij}$  components:

$$\sigma_{ij} = -p\delta_{ij} + \tau_{ij} \quad (4.3)$$

where  $\delta_{ij}$  is the Kronecker delta function. Defining the strain rate

$$\dot{\epsilon}_{ij} = \frac{1}{2} \left( \frac{\partial u_i}{\partial x_j} + \frac{\partial u_j}{\partial x_i} \right) \quad (4.4)$$

the rate of work integral can be written

$$\int_V \sigma_{ij} \frac{\partial u_i}{\partial x_j} dV = \int_V (-p\dot{\epsilon}_{ii} + \tau_{ij}\dot{\epsilon}_{ij}) dV \quad (4.5)$$

The first term on the right-hand side of (4.5) represents the increase in internal energy due to changes in volume, while the second term represents strain energy dissipated by shearing of the material.

At this point, we make the simplifying assumptions that the material is incompressible,  $\dot{\epsilon}_{ii} = 0$ , and that its rheology can be expressed as that of a fluid, with an

effective viscosity  $\eta$  that can be a function of position:

$$\tau_{ij} = 2\eta\dot{\epsilon}_{ij} \quad (4.6)$$

Then the rate at which work is done on the material is

$$\Phi^{\text{vd}} = \int_V \tau_{ij}\dot{\epsilon}_{ij}dV = 2 \int_V \eta\dot{\epsilon}_{ij}\dot{\epsilon}_{ij}dV \quad (4.7)$$

where  $\Phi^{\text{vd}}$  is the total rate of viscous dissipation.

For an isoviscous mantle the fluid deformation within a convecting cell is characterized by a surface plate moving with velocity  $v_p$  and a return flow governed by the free-slip condition at the core-mantle boundary. The resulting viscous flow produces shear stresses that can be determined by analogy to asthenospheric counterflow [e.g., *Turcotte and Schubert*, 1982, pp. 232-236]. The result is  $\tau_{xz} = 3\eta_m v_p (D - z)/D^2$ , where  $\eta_m$  is the mantle viscosity,  $D$  is the mantle thickness, and  $z$  is depth (positive downward). For a cell of length  $L$  we use (4.7) to estimate  $\Phi_m^{\text{vd}}$ , the total rate of viscous dissipation in the mantle

$$\Phi_m^{\text{vd}} = 3\eta_m v_p^2 (A + C_m) \quad (4.8)$$

where  $\Phi_m^{\text{vd}}$ , as for all subsequent expressions for dissipation, is per unit length perpendicular to the direction of flow. Here  $A$  is the aspect ratio of the convecting cell, equal to the greater of  $L/D$  or  $D/L$ . In defining  $A$ , we recognize that for  $L < D$  the dominant flow is similar to the one described above but in the vertical direction and produced by the downgoing slab (also moving with speed  $v_p$ ) and the free-slip boundary associated with the return upwelling. In addition, we recognize that to conserve mass, a return circulation must occur near the two shorter edges of the cell. The variable parameter  $C_m$  in (4.8) accounts for the additional energy dissipated by this circulation and depends on how sharply streamlines of the flow are forced to bend at corners. Simple numerical tests show that (4.8) accurately describes viscous dissipation that occurs in a box with two boundaries that are free-slip and two that

move with velocity  $v_p$ . We also find that  $C_m$  does not depend on the aspect ratio  $A$ .

The remaining term in (4.2) gives the rate at which body forces do work on the fluid. We refer to this term as  $\Phi^{\text{Pe}}$  because, for the mantle, it represents the rate at which gravitational potential energy is released. The net work done by gravity on the hydrostatic component of the density field is zero for a closed convecting cell, so only the horizontally varying component of the density field contributes to  $\Phi^{\text{Pe}}$ . For a Boussinesq fluid whose density varies with temperature,  $\Phi^{\text{Pe}}$  is given by

$$\Phi^{\text{Pe}} = \int_V \rho g \alpha [T_m - T(x, z)] v_z(x, z) dV \quad (4.9)$$

where  $v_z$  is the vertical component of velocity (positive downward),  $T$  is temperature,  $T_m$  is the mantle interior temperature,  $\alpha$  is the thermal expansivity, and  $g$  is the acceleration due to gravity. For slab driven flow, only the descending slab contributes to (4.9). To perform this integral, we must integrate over the temperature profile of the subducting slab, which changes as the slab descends and warms. The heat that warms the slab is lost from the neighboring mantle, so the integral of the temperature profile along horizontal planes should not vary with depth [e.g., *Turcotte and Schubert*, 1982, pp. 176-178]. Thus we can simply use the integral of the surface temperature profile in estimating (4.9). This profile is that of a cooling boundary layer, generated as the lithosphere travels across Earth's surface, and can be represented as an error function [e.g., *Turcotte and Schubert*, 1982, pp. 163-167]:

$$T(z) = \Delta T \operatorname{erf}(z/h_s) + T_s \quad (4.10)$$

where  $T_s$  is the temperature at the surface,  $\Delta T = T_m - T_s$  is the temperature difference between the mantle and the surface, and  $h_s$  is the thickness of subducting lithosphere, defined here in terms of the time  $t_c$  during which the boundary layer has cooled:

$$h_s = 2\sqrt{\kappa t_c} = 2\sqrt{\kappa L/v_p} \quad (4.11)$$

where  $\kappa$  is the thermal diffusivity. Then the total rate of potential energy release

provided by the slab is, in two dimensions

$$\Phi^{\text{pe}} = \rho g \alpha \Delta T v_z l_s \int_0^\infty \operatorname{erfc}\left(\frac{z}{h_s}\right) dz = \frac{\rho g \alpha \Delta T v_p l_s h_s}{\sqrt{\pi}} \quad (4.12)$$

where  $l_s$  is the length of the subducted portion of the slab and we have assumed that the slab velocity is the same as the surface plate velocity  $v_p$ .

The energy balance given by (4.2) is then simply a balance between viscous dissipation and potential energy release, and can be simplified to  $\Phi_m^{\text{vd}} = \Phi^{\text{pe}}$ . Equating these terms using (4.8) and (4.12) yields an expression for the plate velocity:

$$v_p = \frac{\rho g \alpha \Delta T h_s l_s}{3\sqrt{\pi} \eta_m (A + C_M)} \quad (4.13)$$

Combining (4.13) and (4.11), setting  $l_s = D$  and  $L > D$ , and solving for  $v_p$  yields

$$v_p = \left(\frac{4\kappa L}{9\pi}\right)^{1/3} \left(\frac{\rho g \alpha \Delta T D}{\eta_m}\right)^{2/3} \left(\frac{L}{D} + C_m\right)^{-2/3} \quad (4.14)$$

This expression for velocity is a variation of a similar expression given by standard boundary layer theory [*Turcotte and Schubert*, 1982, p. 282]. The differences arise in our estimate of the viscous dissipation in (4.8), where we assume that the boundary condition at the mantle's base is free slip and that a slab's velocity is equal to that of its attached surface plate. For a more complicated system with a strong lithosphere that subducts, the added viscous dissipation in the subduction zone should serve to slow the plate by adding terms to the denominator of (4.13). To determine the influence of the subduction zone, we have developed a finite element model of a convecting system that specifically includes a subduction zone.

### 4.3 Finite Element Model

Various numerical parameterizations of a subduction zone have been used to study a variety of problems. These are generally either local studies designed to investigate the dynamics of the subduction zone itself [e.g., *Gurnis and Hager*, 1988; *Houseman*

and Gubbins, 1997; Melosh and Raefsky, 1980; Toth and Gurnis, 1998; Zhang *et al.*, 1985; Zhong and Gurnis, 1994] or large-scale studies designed to look at the effect of various parameterizations of subduction zones on mantle convection of a global scale [e.g., Bercovici, 1995; Bunge and Richards, 1996; Davies, 1989; Hager and O'Connell, 1981; King and Hager, 1994; King *et al.*, 1992; Puster *et al.*, 1995; Zhong and Gurnis, 1995a, b]. Due to computational constraints, the local studies generally have finer spatial resolution than the global models and thus can more realistically incorporate some of the more detailed structures of a subduction zone. In particular, *Houseman and Gubbins* [1997], *Melosh and Raefsky* [1980], and *Zhang et al.*, [1985] assign a realistic curved geometry to an isolated subducting plate and look at the bending of that plate as it descends. *Zhong and Gurnis* [1994] and *Zhong et al.* [1998] also introduce a fault zone into an otherwise regular grid in an effort to parameterize the interaction between subducting and overriding plates. Finally, *Toth and Gurnis* [1998] allow a fault zone's geometry to evolve in response to dynamical forces associated with the initiation of subduction.

Detailed local models of subduction zones demand fine numerical resolution and complex grid geometry, so it is difficult to incorporate these models into larger-scale global models. To get around this problem, the detailed structure of the subduction zone is generally parameterized in a simple way in an effort to mimic its effects on mantle flow. Several methods have been used. One is to impose piecewise continuous velocity boundary conditions at the surface to force plate-like behavior [e.g., *Hager and O'Connell*, 1981; *Davies*, 1988; *Bunge and Richards*, 1996]. Another approach is to implement plates by combining strongly temperature-dependent viscosity with low-viscosity weak zones that represent plate boundaries [e.g., *Davies*, 1989; *Gurnis and Hager*, 1988; *King and Hager*, 1990; *Puster et al.*, 1995]. Both approaches, while indeed allowing the plates to move in a plate-like fashion, do not take into account the detailed structure of the subduction zone and its dynamics. A few studies include a fault zone that can support shear stresses and allow differential displacements across its width [e.g., *Toth and Gurnis*, 1998; *Zhong and Gurnis*, 1994, 1995a, b; *Zhong et al.*, 1998]. This fault zone parameterizes the interaction between the subducting

and overriding plates and allows for more realistic subduction geometry, in that one plate overrides another and the entire thermal buoyancy of the subducting plate is incorporated into driving convection. These studies, however, do not specifically treat the deformation within the lithosphere as it subducts. This deformation may be important in resisting plate motions, so a more complete analysis of a subduction zone's effect on mantle flow is needed.

In this study we incorporate the important features of local subduction models in a larger-scale convecting system. In particular, we include a smoothly bending subducting slab and an adjacent fault zone in a viscous model of a single convection cell. Both are modeled as viscous fluids in a finite element calculation using ConMan, a finite element code that solves the coupled thermal diffusion and incompressible Navier-Stokes equations for both Newtonian and non-Newtonian rheology [*King et al.*, 1990]. The finite element grid we used includes a lithosphere, mantle, and viscous fault zone, as shown in Figure 4.1. Its length  $L$  is 1500 km, and its depth  $D$  is 1200 km.

An accurate representation of deformation in the subducting slab is facilitated in the design of our finite element grid. The curved surface of the slab is parallel to the direction of its descent into the mantle, allowing it to flow into the mantle in a smooth, continuous fashion, as real slabs do in Earth. A rectangular grid of comparable resolution, which could have been more easily implemented, would not allow this type of slab behavior because the slab edges would consist of corners in the grid, which would alter its flow. The surface of the slab is drawn so that the vertical component of the slab velocity at each point increases as the error function of the arc length around the slab, as described by *Melosh and Raefsky* [1980]. We use a slab dip angle of  $90^\circ$  and a radius of curvature  $R$  of 240 km. This surface describes the curved upper surface of the subducting slab. The rest of the grid, which represents both the lithosphere and mantle, is filled in below this surface as shown in Figure 4.1 and is assigned a temperature-dependent mantle viscosity  $\eta_m$ . Free-slip is imposed along all horizontal and vertical surfaces, and all corners are pinned.

The interaction between the subducting and overriding plates is parameterized

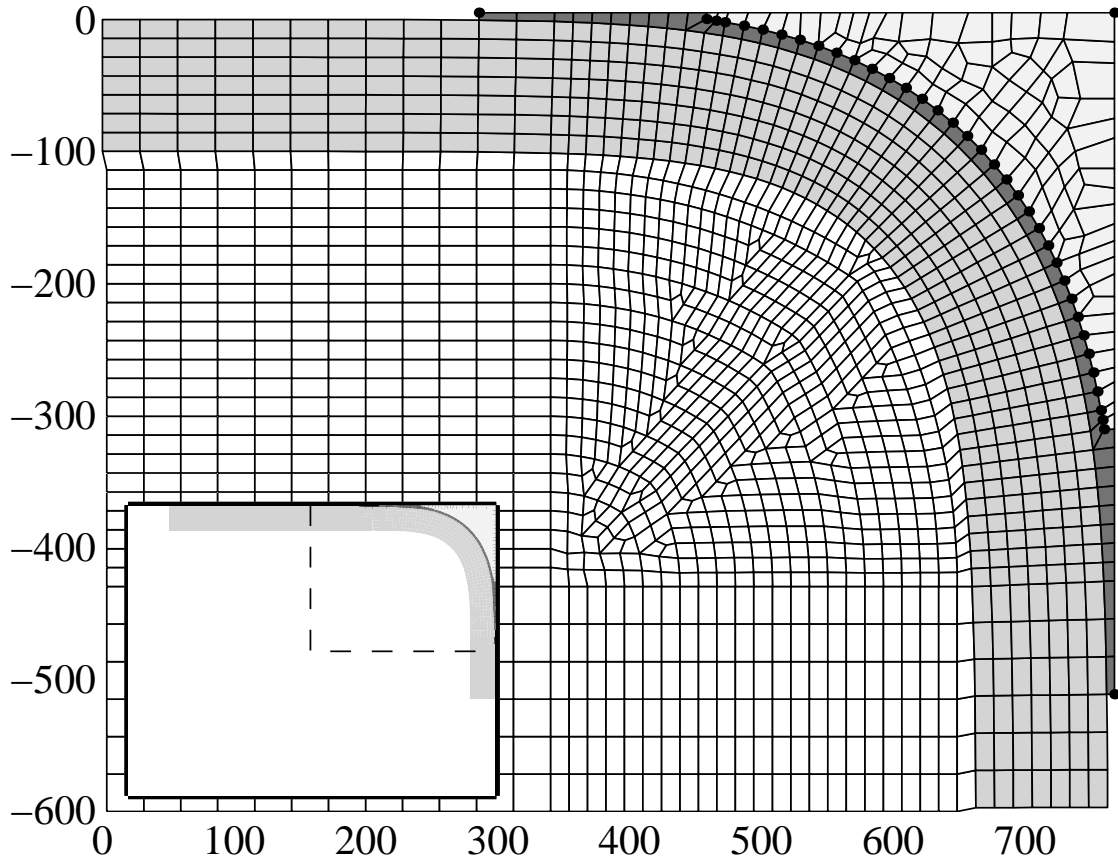


Figure 4.1: The finite element grid used. Shown in expanded detail is the gridding of the subduction zone. This region is highlighted on a schematic of the full finite element grid (inset). The portion of the grid that is not detailed here has a regular geometry and allows a return circulation to the subducting region. The shaded regions represent, from lower left to upper right, the mantle, subducting lithosphere, fault zone, and overriding arc-wedge region. The lithosphere is differentiated from the mantle by temperature alone. Flow boundary conditions are free slip along all grid edges. The large dots represent nodes that are pinned to zero velocity. Distances shown are in kilometers.

by a viscous fault zone one element wide, bounded above by an overriding arc-wedge region whose lower boundary is pinned (Figure 4.1). We use a fault zone of length  $l_f = 782$  km and width  $w_f = 10.7$  km and assign a temperature-independent viscosity  $\eta_f$ , which allows the fault to support shear stress. The shear strain rate across the fault zone is given by  $\dot{\epsilon}_f = \frac{1}{2}v_p/w_f$ , so the shear stress within the fault zone  $\tau_f$  is given by

$$\tau_f = 2\eta_f\dot{\epsilon}_f = \eta_f\frac{v_p}{w_f} \quad (4.15)$$

The strength of a viscous fault zone, represented by the stress it can support, is thus a function of both the imposed viscosity and the velocity of the subducting plate. Real fault zones are not, of course, composed of viscous fluids but of rocks that can support some degree of frictional shear stress. Our viscous fault zone supports shear stresses between the subducting plate and the overriding wedge and thus models this essential aspect of a real fault zone.

The overriding wedge region (Figure 4.1) is also a viscous fluid with a viscosity 100 times that of the mantle, but it does not participate in the main convective flow. Instead, free-slip boundary conditions along the grid edges allow a small circulation of material between the fault zone and the wedge. This circulation is minor and does not affect the dynamics of the subducting plate system, as demonstrated below.

We assign an error function temperature profile to the oceanic lithosphere as given by (4.10), using  $T_s = 273$  K,  $\Delta T = 1200^\circ\text{C}$ ,  $\kappa = 1$  mm<sup>2</sup> s<sup>-1</sup>, and a preimposed cooling time  $t_c$ . Initially, this temperature profile is imposed across the entire surface of the grid. Velocity boundary conditions along the surface of the oceanic plate are used to advect this temperature profile into the mantle, where thermal diffusion allows some warming of the slab as it descends. Because the finite element grid is not long enough for significant thickening of the thermal boundary layer to occur as it traverses the box, the imposed cooling time  $t_c$  dictates the approximate thickness of the slab, as in (4.11).

The cold temperatures of the oceanic lithosphere are responsible for its increased strength relative to the mantle below. Temperature-dependent viscosity  $\eta(T)$  is gen-

erally given for dislocation flow as [e.g., *Kohlstedt et al.*, 1995]

$$\eta(T) = \eta_m \exp\left(\frac{E_a}{RT} - \frac{E_a}{RT_m}\right) \quad (4.16)$$

where  $R = 8.31 \text{ J mol}^{-1} \text{ K}^{-1}$  is the universal gas constant,  $E_a$  is the activation energy, and mantle temperature  $T_m$  yields mantle viscosity  $\eta_m$  [*King*, 1991]. This viscosity law is only applied to the lithosphere and mantle, and a maximum viscosity of  $10^4 \eta_m$  is enforced. Although the above viscosity law does not account for the variety of deformation mechanisms that may occur in the subducting lithosphere, we account for the strengthening or weakening effects of these mechanisms by allowing  $E_a$  to vary. Thus (4.16) can be thought of as defining the effective viscosity of the lithosphere.

Once the velocity boundary conditions have advected the temperature field to depth, they are replaced by free-slip boundary conditions. The temperature field then provides negative buoyancy with which the slab can drive mantle flow. This is achieved by making the Boussinesq approximation and by imposing a nonzero coefficient of thermal expansion,  $\alpha$ , everywhere except for the overriding wedge. We allow the dense slab to drive convection until a thermally consistent steady state model of mantle flow is achieved. In other words, the plate descends under its own weight with a constant velocity  $v_p$ , and the thermal buoyancy of the plate is determined by the descent of a slab with this same velocity. We calculate this steady state solution using a fault zone viscosity of  $\eta_m/100$  and an activation energy of  $E_a = 100 \text{ kJ mol}^{-1}$ . The latter value is smaller than is generally found for olivine in laboratory experiments, but *Christensen* [1984a] shows that the effects of stress-dependent viscosity can be approximated in calculations with Newtonian viscosity by decreasing  $E_a$ . In any case, this steady state solution is used only as a starting point for the models described below in which we allow  $\eta_f$  and  $E_a$  to vary.

It is potentially difficult to force strong lithosphere into or away from the corners of the finite element grid. To prevent this difficulty, we apply temperature boundary conditions to prevent high-viscosity material from nearing the corners (Figure 4.1, inset). When the slab descends deeper than 800 km depth, its temperature is set to

$T_m$ , thus eliminating its strength and thermal buoyancy below this depth. Similarly, as the plate pulls away from the mantle upwelling opposite the descending slab, mantle viscosities are imposed for the first 200 km of the plate. Buoyancy, however, is still controlled by the temperature distribution, which is set to mimic that of a ridge by using (4.10) and allowing  $t_c$  to increase linearly from zero to its full value at 200 km. In this way, we more realistically generate the small pushing force derived from the horizontal juxtaposition of buoyant mantle and dense lithosphere, while still allowing the slab to easily pull away from the edge of the grid.

The importance of the slab and fault zone should depend on their rheology. To see how they do, we vary the strength of the fault zone by changing its viscosity  $\eta_f$  and the effective viscosity of the lithosphere by changing the activation energy,  $E_a$ , associated with temperature dependence in (4.16). The steady state buoyancy field is used to drive flow for one time step to test the system's response to each new rheology. We record the plate velocity and the total viscous dissipation the mantle, lithosphere, fault zone, and overriding wedge. The lithosphere is distinguished from the mantle by temperature; elements with average temperatures  $< 0.9\Delta T + T_s$  are considered lithosphere.

## 4.4 Nondimensionalization

The activation energy  $E_a$  determines how viscosity varies with depth in the lithosphere. To determine how the geometry and rheology of the subduction zone affect its importance to the convecting system, it is useful to estimate an effective viscosity of the entire lithosphere for a given activation energy. To do this, we use an averaging method suggested by *Parmentier et al.* [1976] in which viscosity is weighted by the square of the second invariant of the strain rate tensor  $\dot{\epsilon}$  and then averaged over volume:

$$\bar{\eta} = \frac{\int_V \eta \dot{\epsilon}^2 dV}{\int_V \dot{\epsilon}^2 dV} \quad (4.17)$$

We have performed experiments with both Newtonian and strain-rate-dependent rheology and have found that our results, when expressed in terms of this definition of

effective viscosity, are independent of the type of rheology applied. As a result, we can define an effective viscosity that is the result of either Newtonian or non-Newtonian rheology in a bending lithosphere. In addition, it should be possible to account for brittle behavior by applying a highly non-Newtonian (plastic) rheology, which approximates the effects of a yield stress.

We nondimensionalize the lithosphere and fault zone viscosities by the mantle viscosity:

$$\eta'_l = \frac{\bar{\eta}_l}{\bar{\eta}_m} \quad \eta'_f = \frac{\bar{\eta}_f}{\bar{\eta}_m} \quad (4.18)$$

where overbars indicate effective viscosities calculated using (4.17) and primes indicate dimensionless quantities. We note that a typical velocity is given by  $v_{p0} = 2\dot{\epsilon}_0 h_s = \tau_0 h_s / \bar{\eta}_m$ , where  $\dot{\epsilon}_0$  is a typical strain rate and  $\tau_0$  is a typical stress. Using  $\tau_0 = \rho g \alpha \Delta T l_s$ , we nondimensionalize velocity as

$$v'_p = \frac{v_p}{(\rho g \alpha \Delta T h_s l_s / \eta_m)} \quad (4.19)$$

Because dissipation in the fault zone is related to both its length  $l_f$  and the shear stress it supports,  $\tau_f$ , it is useful to express the fault zone strength as the product of these quantities, made dimensionless using  $\tau_0$  and  $h_s$ :

$$(\tau_f l_f)' = \frac{\tau_f l_f}{\rho g \alpha \Delta T h_s l_s} \quad (4.20)$$

Combining (4.15), (4.18), (4.19), and (4.20), we find

$$(\tau_f l_f)' = \eta'_f v'_p l_f / w_f \quad (4.21)$$

To calculate  $(\tau_f l_f)'$ , we areally average the shear stress in the fault zone elements, multiply by  $l_f$ , and nondimensionalize this quantity using (4.20). The result is generally larger than values predicted using (4.21) by roughly 20%. Runs in which the subducting plate is significantly slowed by the lithosphere's strength yield fault zone stresses that are even larger, probably because the stress is less accurately represented

by the shearing given by (4.15) if  $v_p$  is small. In any case, the fact that (4.20) and (4.21) agree as well as they do over orders of magnitude change in both fault zone and lithosphere viscosity indicates that we can accurately represent a fault zone in a viscous way.

## 4.5 Finite Element Results

We have run the finite element code for a range of lithosphere and fault zone strengths for plate thicknesses of 57, 100, and 157 km. As a result, we are able to determine how the dimensionless plate velocity varies with  $\eta'_l$ ,  $(\tau_f l_f)'$ , and  $h_s$  (Figures 4.2a, 4.3a, and 4.4a). In the nondimensionalization we assume an effective slab length of  $l_s = 700$  km, which ignores any contribution from the upper 100 km of the finite element grid. This is reasonable because the driving buoyancy of the slab is determined by horizontal variations in density, which are small near the surface due to the slab's nearly horizontal orientation there (Figure 4.1).

An isoviscous convecting system with an aspect ratio of  $A = L/D = 1500/1200 = 1.25$  should produce a dimensionless velocity of  $v'_p = 0.06$ , as shown by a comparison of (4.13) and (4.19) if  $C_m = 2$ , as we estimate later. The finite element results show that  $v'_p$  is less than this value for all lithosphere and fault zone viscosities shown but is close to this isoviscous limit for a weak, thin, lithosphere and a weak fault zone (Figure 4.2a). Thus a strong lithosphere or fault zone significantly slows a plate. Thick plates are slowed more than thin plates for a given lithosphere viscosity and fault strength (compare Figures 4.2a, 4.2b, and 4.2c), especially for plates with high lithospheric viscosity.

To show that it is indeed the bending of the slab and the shearing of the fault zone that act in slowing the plate, we plot the percentage of the total viscous dissipation that occurs in each of the mantle (Figures 4.2b, 4.3b, and 4.4b), lithosphere (Figures 4.2c, 4.3c, and 4.4c), and fault zone (Figures 2d, 4.3d, and 4.4d) as a function of dimensionless lithosphere viscosity and fault strength for each of the three plate thicknesses studied. The fraction of the viscous dissipation that occurs in the wedge

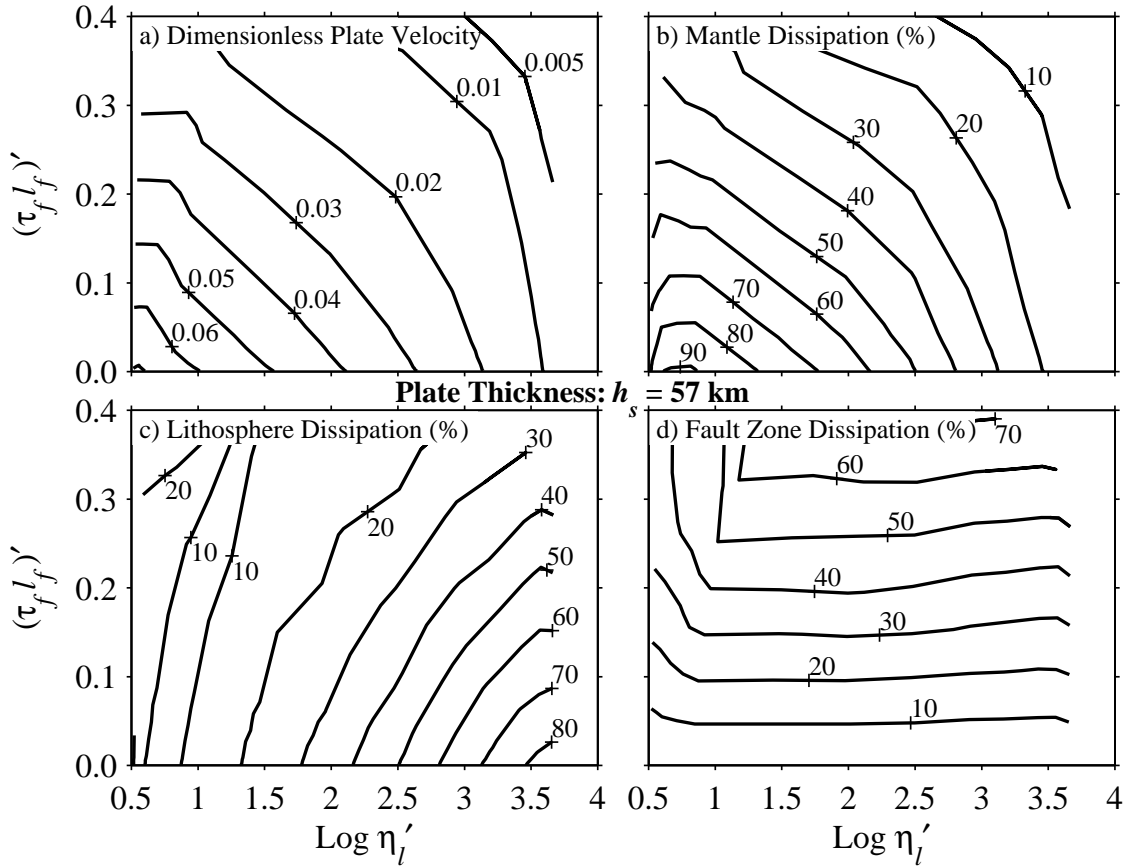


Figure 4.2: Results from the finite element model for a plate thickness of  $h_s = 57 \text{ km}$ , plotted as a function of dimensionless lithosphere viscosity  $\eta'_l$  given by (4.18) and the dimensionless fault strength  $(\tau_f l_f)'$  given by (4.20). Shown are (a) the dimensionless plate velocity  $v'_p$ , given by (4.19), and the percentage of the total viscous dissipation that occurs in the (b) mantle, (c) lithosphere, and (d) fault zone. For comparison, these regions represent 91%, 7%, and 0.5% of the total area of the finite element grid.

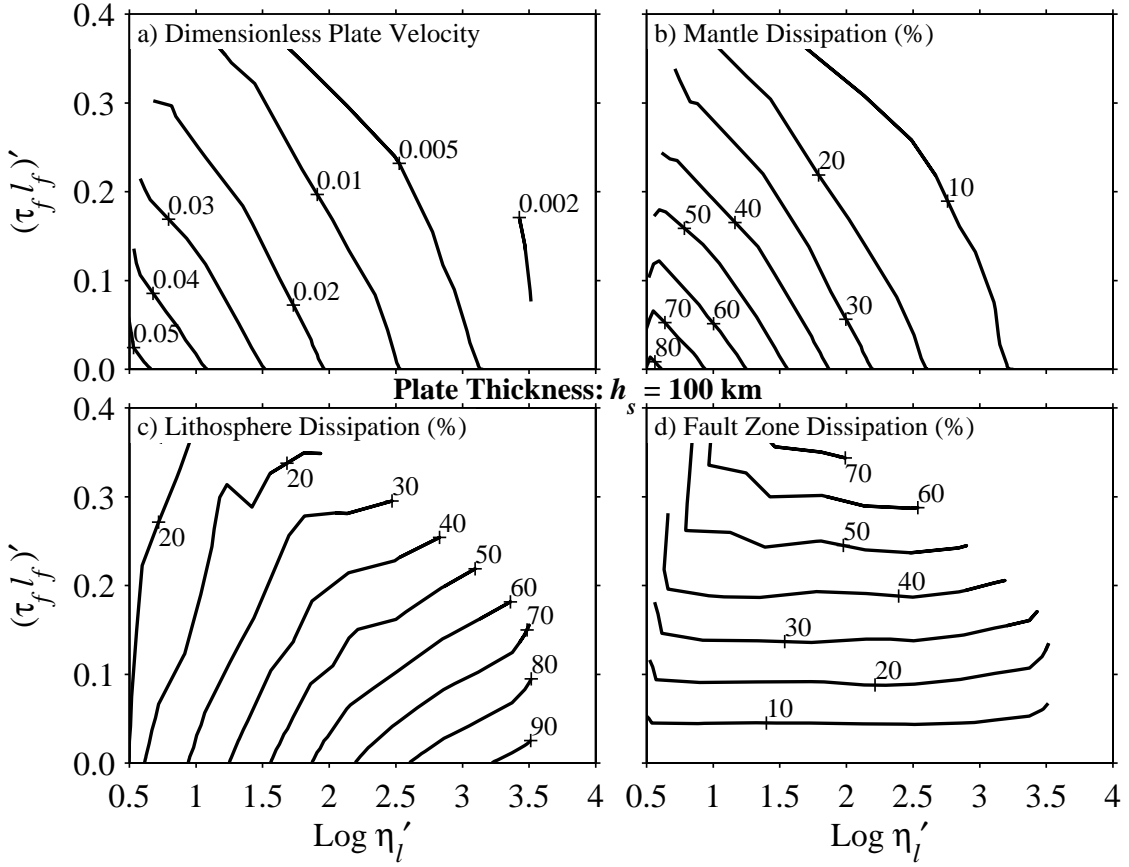


Figure 4.3: Similar to Figure 4.2, for a plate thickness  $h_s = 100$  km. The mantle, lithosphere, and fault zone represent 87%, 11%, and 0.5% of the total area, respectively.

region is everywhere less than  $< 0.5\%$  of the total and thus is insignificant. Included in the figure captions is the fraction of the total area of the finite element grid each region represents. In every case, the fraction of the viscous dissipation that occurs in the mantle is smaller than its areal fraction. Instead, the lithosphere or fault zone dissipate more than their share of the total.

In general, as the fault zone strength increases, the plate velocity decreases and the proportion of dissipation in the fault zone increases, indicating that an increased resistance in the fault zone slows the plate. We also observe the same general trend of decreased plate velocities and increased dissipation in the lithosphere as either the thickness or viscosity of the lithosphere increases. The fraction of dissipation in

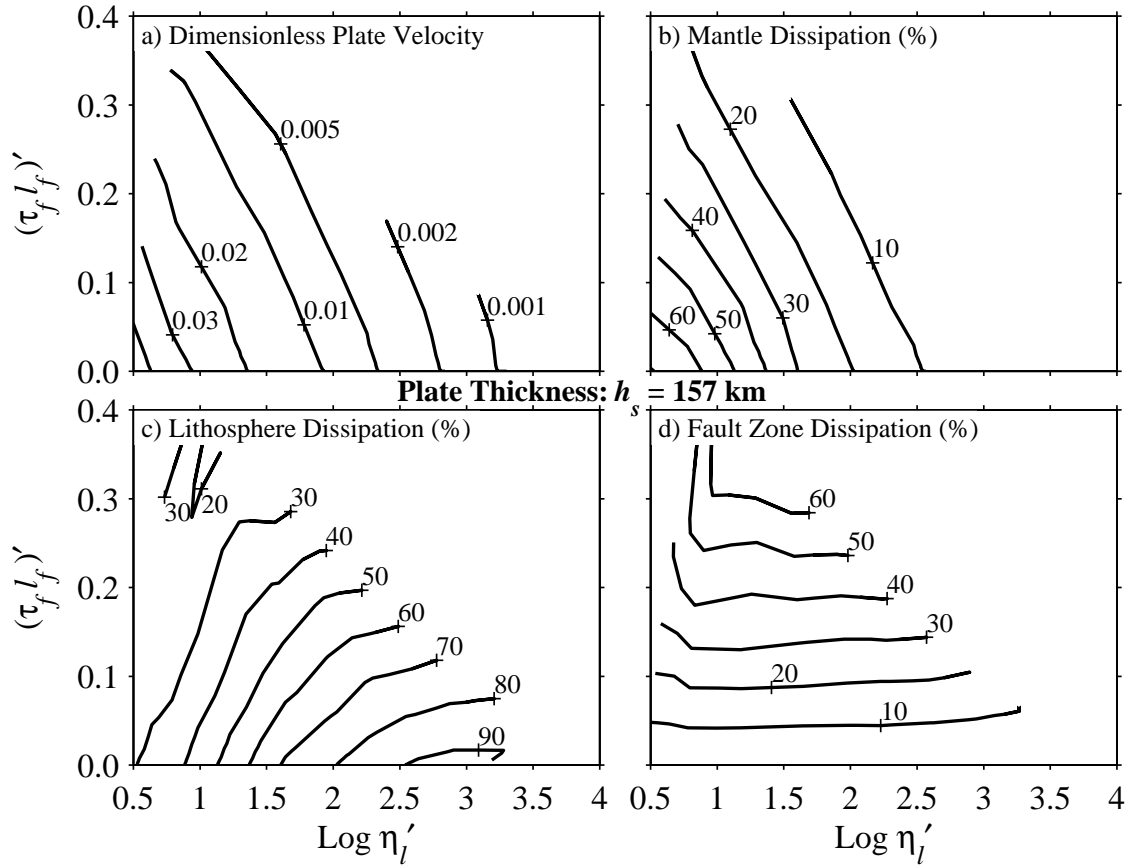


Figure 4.4: Similar to Figure 4.2, for a plate thickness  $h_s = 157$  km. The mantle, lithosphere, and fault zone represent 82%, 16%, and 0.5% of the total area, respectively.

the lithosphere increases with decreasing lithosphere strength, however, if the fault zone is strong but the lithosphere is weak. This is because a strong fault zone acts to pin the surface of the slab to the overriding wedge. If the slab is itself weak, significant shearing is permitted within the slab, causing viscous dissipation in the slab to increase. This motion, however, is not plate-like because the fault zone does not accommodate motion of the subducting plate past the overriding wedge. The fault zone, by definition, must be weaker than the subducting plate.

## 4.6 Theoretical Prediction of Plate Velocity

The finite element results show that the plate velocity decreases significantly from its expected isoviscous value when a strong lithosphere or fault zone are present. Because the expression for the plate velocity (4.13) arises from a balance between viscous dissipation and potential energy release, it is clear that the expression for this balance becomes incorrect as we increase the strength of the lithosphere or fault zone. The expression for potential energy release (4.12) should not be altered by this change, but the expression for viscous dissipation should include the dissipation that occurs in the fault zone and the lithosphere. We attempt to combine the viscous dissipation in these regions with that of the mantle in (4.8) to obtain an expression for velocity similar to (4.13). To do this, we first characterize fault zone and lithosphere dissipation.

### 4.6.1 Fault Zone Dissipation

The pattern of viscous dissipation in the fault zone is shown by Figure 4.5 for a strong fault zone with an intermediate lithosphere viscosity. It is clear that the largest rate of viscous dissipation is found within the elements of the fault zone and is typically between 50 and 100 times the mean value for the entire finite element grid. For a plate velocity of  $v_p = 10 \text{ cm yr}^{-1}$  and the mantle parameters given later, we estimate, using (4.12), an average potential energy release of  $1.7 \times 10^{-8} \text{ W m}^{-3}$  for a convecting cell. Assuming a specific heat of  $C_p = 1100 \text{ J kg}^{-1} \text{ K}^{-1}$ , the concentration of this heating by a factor of 100 within the fault zone should cause temperatures there to increase by  $75^\circ\text{C}$  in the 5 Myr it takes for a subducting material to pass through 500 km of subduction zone. This heating may weaken the fault somewhat but should be primarily carried away by thermal diffusion into the adjacent cold slab.

We have shown that the decrease in velocity from  $v_p$  to zero across the fault zone of width  $w_f$  and area  $l_f w_f$  generates a shear stress  $\tau_f$  given by (4.15). If  $\tau_f$  is nearly uniform along the fault's length, the dissipation in the fault zone  $\Phi_f^{\text{vd}}$  can be expressed

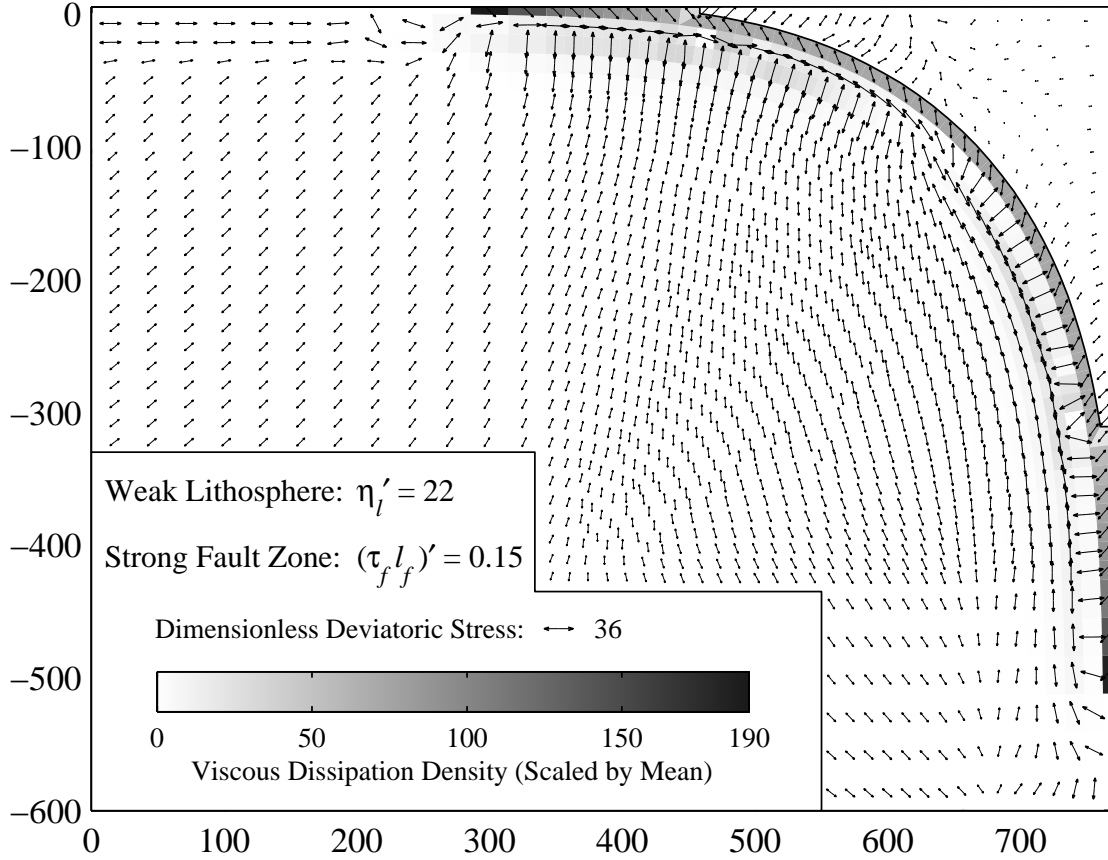


Figure 4.5: Distribution of viscous dissipation (gray shades) and the directions of most extensile deviatoric stress (arrows) for  $h_s = 100$  km and viscous parameters that yield a relatively weak lithosphere and a relatively strong fault zone. Here,  $\eta_l' = 22$ ,  $(\tau_f l_f)' = 0.15$ , and  $v_p' = 0.018$ . For reference, the upper surface of the fault zone is represented as a solid line. The density of viscous dissipation is shown as a multiple of the average value for the entire finite element grid. The length of arrows is scaled by the log of the amplitude of the dimensionless deviatoric stress,  $\tau' = \tau / (\rho g \alpha \Delta T h_s)$ , and stresses a factor of  $10^5$  smaller than the maximum stress are given zero length. The percentages of the total viscous dissipation in the mantle, lithosphere, and fault zone are 36%, 27%, and 37%.

using (4.7):

$$\Phi_f^{\text{vd}} = \tau_f v_p l_f \quad (4.22)$$

Neither the width of the fault zone  $w_f$  nor its viscosity,  $\eta_f$ , are used in this estimation of dissipation. Faults in real subduction zones are not viscous but may exhibit brittle or plastic rheology and thus should support some degree of shear stress over some length, so we can still estimate their contribution to the total viscous dissipation using (4.22).

### 4.6.2 Lithosphere Dissipation

The lithosphere exhibits a more complicated pattern of dissipation than does the fault zone, as is shown in Figure 4.6 for a strong lithosphere and a weak fault zone. There appear to be four primary regions of contribution to the total dissipation. As the slab begins to subduct, one region near the top of the slab exhibits extensional stresses along its length, while another region below it is under horizontal compression. This pattern is reversed as the slab exits the curved part of the subducting slab. These stresses are similar to fiber stresses in a bending elastic plate, as described by *Turcotte and Schubert* [1982, pp. 112-115]. As the slab begins to descend, it must deform into a bent shape, which forces the surface of the slab to expand while its base contracts. As the slab continues to descend, it must unbend from a curved shape into a straight one. The recovery of this straightened shape requires undoing the inelastic deformation that originally bent the slab. Thus the top surface of the slab contracts while the bottom surface expands. This stress pattern matches the one observed in Figure 4.6 and generates an amplification of viscous heating by up to a factor of 100 (Figure 4.6). If we assume that the average heating of slab material as it travels through the subduction zone is half of this, we expect the slab to only warm by  $35^\circ\text{C}$ , which should not significantly affect its material strength.

We estimate the dissipation associated with the observed stress pattern by analyzing the bending and unbending deformation. It can be shown using similar triangles [*Turcotte and Schubert*, 1982, pp. 114-115] that the horizontal strain  $\epsilon_{xx}$  associated

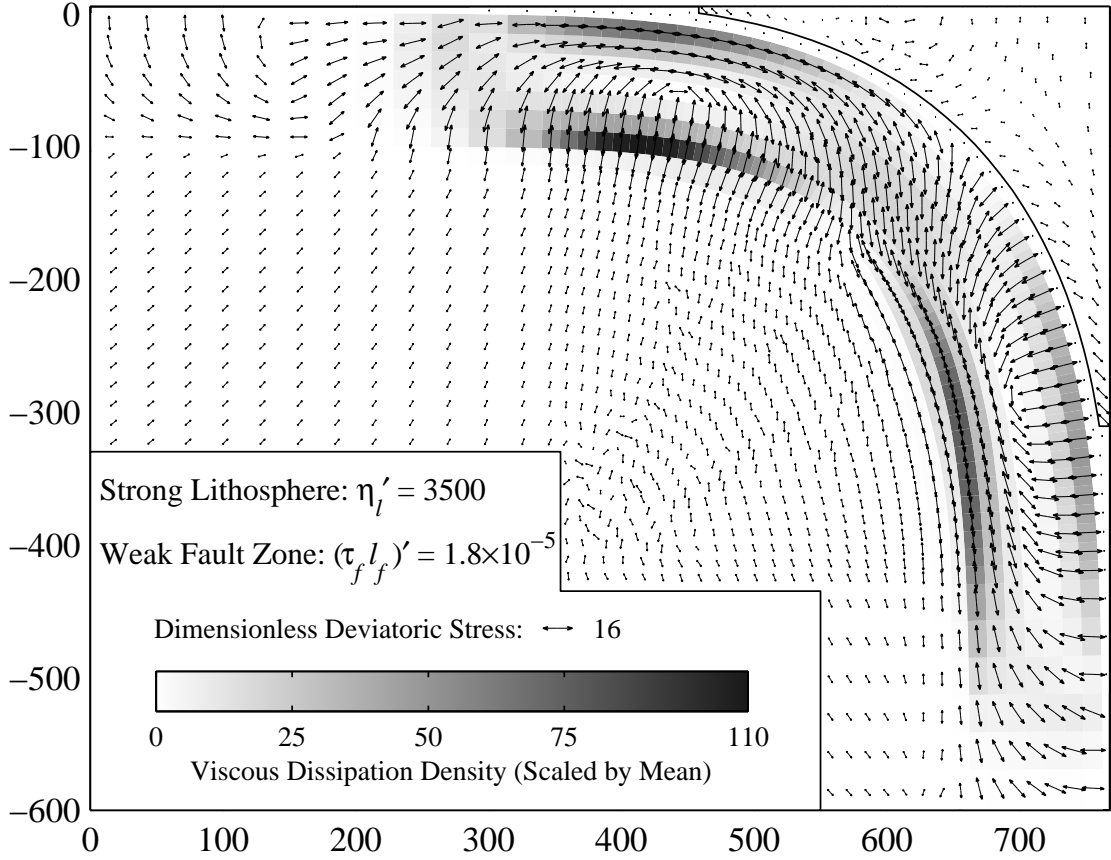


Figure 4.6: Similar to Figure 4.5, for  $h_s = 100$  km and viscous parameters that yield a relatively strong lithosphere and a relatively weak fault zone. Here,  $\eta_l' = 3500$ ,  $(\tau_f l_f)' = 1.8 \times 10^{-5}$ , and  $v_p' = 0.0021$ . The percentages of the total viscous dissipation in the mantle, lithosphere, and fault zone are 7%, 93%, and 0.003%.

with bending is

$$\epsilon_{xx} = \frac{\Delta l_c}{l_c} = \frac{y}{R} \quad (4.23)$$

where  $\Delta l_c$  is the change in length  $l_c$  of a fiber in the curved part of the slab,  $y$  is the distance from the centerline of the slab, and  $R$  is the radius of curvature with which the bending occurs. We can obtain a strain rate by dividing by a typical timescale for bending. In this case,  $l_c/v_p$  is an appropriate timescale because the slab is being strained as it is being pulled through the curved part of the subduction zone.

However,  $l_c$  is proportional to  $R$ , so we can approximate the strain rate as

$$\dot{\epsilon}_{xx} \sim \frac{v_p}{R} \frac{y}{R} \quad (4.24)$$

Combining (4.7) and (4.24), the viscous dissipation in the lithosphere,  $\Phi_l^{\text{vd}}$ , is

$$\Phi_l^{\text{vd}} \sim l_c \eta_l \int_{-h_s/2}^{h_s/2} \left( \frac{v_p}{R} \frac{y}{R} \right)^2 dy \quad (4.25)$$

Performing this integral and using the fact that  $l_c$  is proportional to  $R$ , we find

$$\Phi_l^{\text{vd}} = C_l v_p^2 \eta_l \left( \frac{h_s}{R} \right)^3 \quad (4.26)$$

where we have introduced the constant  $C_l$  in which we incorporate all constants of proportionality and integration that arise in the derivation. Thus we find that the lithospheric dissipation depends on the cube of the ratio of the thickness of the slab to its radius of curvature.

### 4.6.3 Expression for Plate Velocity

The sum of the dissipation rates for each of the mantle, fault zone, and lithosphere yields the total dissipation in the convecting system, which should equal its rate of potential energy release, as shown by (4.2). Thus

$$\Phi^{\text{pe}} = \Phi_m^{\text{vd}} + \Phi_f^{\text{vd}} + \Phi_l^{\text{vd}} \quad (4.27)$$

Combining (4.8), (4.12), (4.22), and (4.26) and solving for the plate velocity, we find

$$v_p = \frac{C_s \rho g \alpha \Delta T l_s h_s - C_f \tau_f l_f}{3\eta_m (A + C_m) + C_l \eta_l (h_s/R)^3} \quad (4.28)$$

where we assign  $C_s = 1/\sqrt{\pi}$  and introduce the constant  $C_f$ , which should be close to unity, to account for possible inconsistencies between the theory used to derive (4.28) and the finite element results. If we apply the nondimensionalizations we have

previously developed in (4.18), (4.19), and (4.20) to (4.28), we find

$$v_p' = \frac{C_s - C_f (\tau_f l_f)'}{3(A + C_m) + C_l \eta_l' (h_s/R)^3} \quad (4.29)$$

We compare the dimensionless velocity observed in the finite element results (Figures 4.2a, 4.3a, and 4.4a) to the velocities predicted by (4.29) in Figure 4.7. This comparison requires us to estimate the constants  $C_m$ ,  $C_l$ , and  $C_f$ . To do this, we look first at the velocity curve for  $h_s = 157$  km,  $\log \eta_l' > 2$ , and  $(\tau_f l_f)' = 0.005$  (Figure 4.7a). In this region, lithosphere dissipation largely determines the velocity, as seen in (4.29) where the second term in the denominator dominates. We find that  $C_l = 2.5$  gives a good match for this portion of the line when  $C_m$  and  $C_f$  are unity. We next determine  $C_m$  by approximately matching this same curve near  $\log \eta_l' = 0.5$ , where the mantle dissipation is most important, and find that  $C_m = 2.5$  gives a good match. Finally, we determine  $C_f$  by matching the curves for  $(\tau_f l_f)' = 0.3$  (Figure 4.7d) where the fault zone is most important, finding  $C_f = 1.2$ .

The results shown in Figure 4.7 show that both the  $h_s = 100$  km and  $h_s = 157$  km curves are well matched between the finite element results and theory. This match is impressive given that it occurs over orders of magnitude variations in the dimensionless lithosphere viscosity and fault zone strength, where the importance of each ranges from negligible to governing. The third set of curves,  $h_s = 57$  km, shows finite element velocities that are consistently larger than predicted, but the match is not unreasonable, and the predictive power of (4.29) does not appear significantly diminished. One explanation for the discrepancy could be that the thinner slab has a longer effective slab length  $l_s$  because more of the curved part of the slab can participate in pulling the slab downward. The result of increasing  $l_s$  is most easily seen by first redimensionalizing both the observed and predicted curves using the previous value of  $l_s$  that we used to nondimensionalize them. This yields the dimensional values of the observed plate velocity, to be matched by (4.28). Using a larger value of  $l_s$  in (4.28) increases the predicted value of  $v_p$  by increasing the driving buoyancy of the plate. Thus assuming a larger value of  $l_s$  for the  $h_s = 57$  km curves

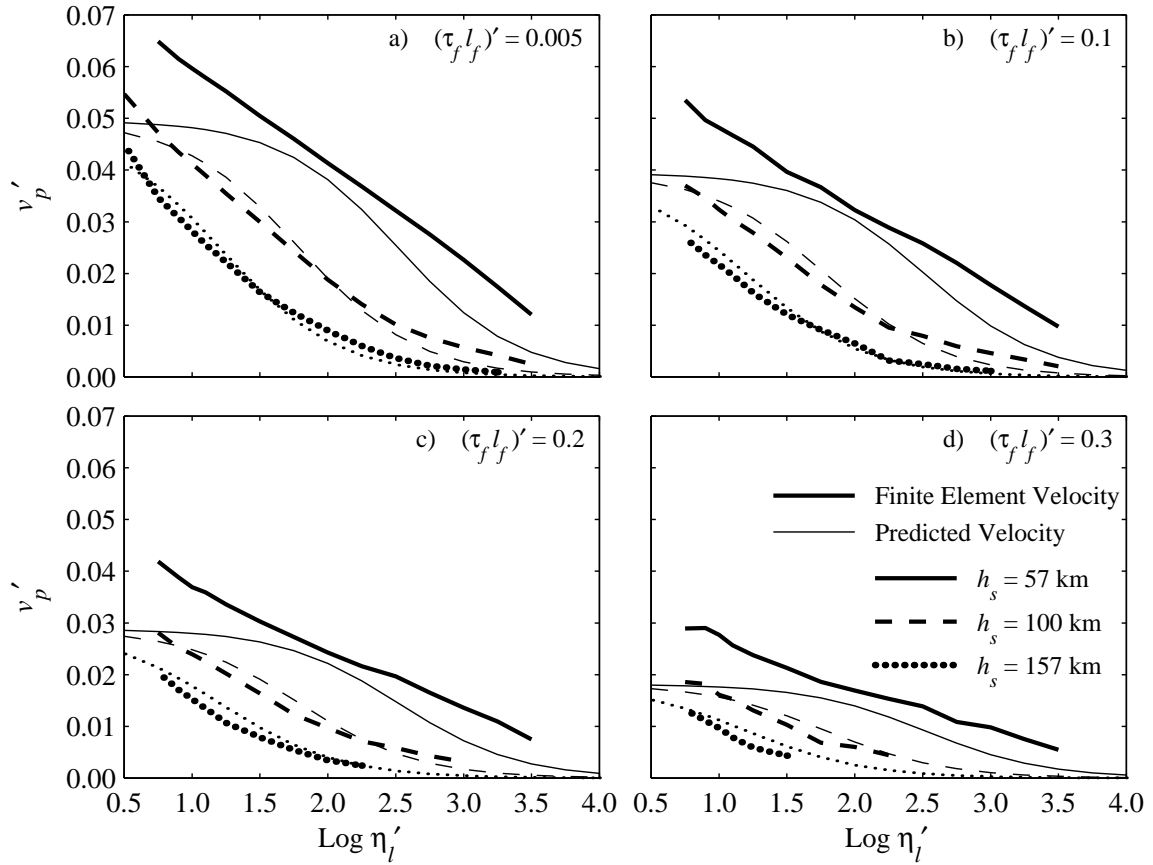


Figure 4.7: A comparison of the dimensionless velocity  $v'_p$  obtained from the finite element calculations (thick lines) to the velocity predicted by theory (thin lines) using (4.29). Velocity is nondimensionalized using (4.19) and is plotted as a function of the log of the dimensionless lithosphere viscosity  $\eta'_l$  for four different dimensionless fault zone strengths  $(\tau_f l_f)'$  and for plate thicknesses of  $h_s = 57, 100,$  and  $157$  km (solid, dashed, and dotted lines). We use  $C_m = 2.5$ ,  $C_f = 1.2$ , and  $C_l = 2.5$  in (4.29), which are estimated as described in the text.

should bring their observed and predicted velocities closer together. This effect will be more pronounced for a strong fault zone because the numerator of (4.28) is smaller so a constant increase in the driving buoyancy should cause a proportionally larger increase in velocity. This could explain the larger discrepancy for the thin plate in Figure 4.7d.

Theory predicts that  $C_f$  should be unity, but it is larger by 20%. One explanation for this discrepancy could be that (4.22) underestimates fault zone dissipation by 20%, requiring a corresponding increase in  $C_f$  to yield the correct dissipation. Another possibility is again a change in the length of the slab,  $l_s$ . Decreasing the slab length by, say, a factor of 1.2 would cause a decrease in the first term in the numerator of (4.28). To prevent a decrease in plate velocity, we could decrease  $C_f$  and  $C_l$  by the same factor and  $C_m$  by a different factor that depends on  $A$ . This would approximately yield  $C_f = 1$ , as predicted by theory, and  $C_m = C_l = 2$ . This group of constants, combined with the new shorter slab length, causes the lines in Figure 4.7 to match as well as they currently do, only at larger dimensionless velocities because they are nondimensionalized with the shorter slab length (4.19). This seems a likely explanation because it involves changing the effective length of the slab, a quantity that is difficult to estimate and may also be responsible for the discrepancies seen for thinner plates. Thus we proceed using  $C_f = 1$  and  $C_m = C_l = 2$ .

## 4.7 Comparison to Observed Plate Velocities

Plates that are attached to subducting slabs move faster than those that are not [e.g., *Forsyth and Uyeda, 1975; Gripp and Gordon, 1990*]. The difference is striking; plates with an attached slab move with velocities between 6 and 9 cm yr<sup>-1</sup> while those without generally move slower than 2 cm yr<sup>-1</sup> when velocities are measured relative to the hotspot reference frame [e.g., *Forsyth and Uyeda, 1975; Gordon and Jurdy, 1986*]. The more rapid motion of slab-bearing plates is thought to indicate that the pull of slabs plays a dominant role in propelling the plates [e.g., *Gripp and Gordon, 1990*].

Earth's slab-bearing plates exhibit a wide range of horizontal length scales, as shown in Table 4.1, where two estimates of the plate length  $L$  are given. If a plate moves with constant velocity and does not change in size, the plate length is given by  $L = A_s v_p$ , where  $A_s$  is the age of the plate as it begins to subduct. Because  $A_s$  varies along the horizontal length of the subduction zone, the ages presented in Table 4.1 are averages determined by taking the length-weighted average of slab ages given by *Jarrard* [1986]. For the Pacific plate, three separate subducting regions are given, as well as their average. Another approximation to the horizontal length scale of the plate is the square root of the area of the plate. It is apparent from Table 4.1 that both approximations for  $L$  are about the same for each plate and that Earth's plates exhibit about an order of magnitude variation in plate length, from 1500 km for the Cocos plate to 10,000 km for the Pacific plate. The velocities associated with these plates, however, are not correlated to these length scales (Table 4.1). All slab-bearing plates, with the exception of the small Juan de Fuca plate, move with absolute velocities between 6 and 9 cm yr<sup>-1</sup>. This consistency of plate velocities is supported by the past history of plate motions. *Gordon and Jurdy* [1986] show that nearly all oceanic plates have moved with velocities between 5 and 9 cm yr<sup>-1</sup> throughout the Cenozoic. Some exceptions include the Kula, Farallon, and Indian plates, which achieved velocities of 11 to 14 cm yr<sup>-1</sup> in the early Cenozoic, and the slow Juan de Fuca plate today.

The lack of a relationship between plate velocity and length is somewhat surprising, because if the resistive forces of plate tectonics depend on the shearing of the underlying mantle, smaller plates should move more rapidly than larger ones [e.g., *Morgan*, 1971]. Thus, if the velocity is given by (4.13), we expect longer plates to be slowed. This, of course, assumes that the driving force of each plate is the same. We do not expect this to be true, because longer plates should have thicker slabs, which will drive them faster. The equilibrium relationship between velocity and plate length is given by (4.14), which has a flatter dependence on  $L$  than does (4.13). This could help explain the lack of variation of  $v_p$  among oceanic plates, but  $v_p$  in (4.14) still depends on  $L$ .

**Table 4.1.** Subducting Plate Data

| Plate                     | Velocity; <sup>a</sup> cm/yr | Subducting Age; <sup>b</sup> Ma | Plate Length, km |                                  |
|---------------------------|------------------------------|---------------------------------|------------------|----------------------------------|
|                           | $v_p$                        | $A_s$                           | $L = A_s v_p$ ,  | $L = \sqrt{\text{Plate Area}}^a$ |
| Cocos                     | 8.6                          | 17                              | 1500             | 1700                             |
| Indian                    | 6.1                          | 105                             | 6400             | 7700                             |
| Juan de Fuca <sup>b</sup> | 3.4                          | 8                               | 300              |                                  |
| Nazca                     | 7.6                          | 51                              | 3900             | 3900                             |
| Pacific                   |                              |                                 |                  |                                  |
| Total                     | 8.0                          | 104                             | 8300             | 10400                            |
| South                     | 8.0                          | 94                              | 8000             | 10400                            |
| Japan                     | 8.0                          | 128                             | 10240            | 10400                            |
| Alaska                    | 8.0                          | 47                              | 3800             | 10400                            |
| Philippine                | 6.4                          | 37                              | 2400             | 2300                             |

<sup>a</sup>From *Forsyth and Uyeda* [1975].

<sup>b</sup>From *Jarrard* [1986].

By including the energy dissipation of the fault zone and lithosphere in the total energy balance of the convecting cell, a new variation of  $v_p$  with  $L$  should result. It is possible that by adjusting the strengths of the lithosphere and fault zone, we can find a new distribution of plate velocities that is consistent with the observation that  $v_p$  does not depend on  $L$ . To determine the range of lithosphere and fault zone strengths in which this occurs, we first express the plate velocity  $v_p$  as a function of plate thickness  $h_s$  using a variation of (4.28) and (4.29):

$$v_p = \frac{\rho g \alpha \Delta T l_s h_0}{\eta_m} \frac{h_s / (h_0 \sqrt{\pi}) - (\tau_f l_f)'}{3(A+2) + 2\eta_l' (h_s/R)^3} \quad (4.30)$$

where we have changed the nondimensionalization of fault zone strength by replacing

$h_s$  by  $h_0$  in (4.20). This is done so that the dimensional value of the fault zone strength does not change with the plate thickness. We let  $h_0$  have a constant value of 100 km, but this value has no physical meaning, since the dimensional fault strength is not dependent on it. We also assume  $\kappa = 10^{-6} \text{ m}^2 \text{ s}^{-1}$ ,  $\rho = 3300 \text{ kg m}^{-3}$ ,  $g = 10 \text{ m s}^{-2}$ ,  $\alpha = 3 \times 10^{-5} \text{ K}^{-1}$ ,  $\Delta T = 1200^\circ\text{C}$ ,  $l_s = 1000 \text{ km}$ , and  $D = 2500 \text{ km}$ . The radius of curvature of the descending slab,  $R$ , is taken to be 200 km, after estimates by *Bevis* [1986] and *Isacks and Barazangi* [1977]. Below, we determine how plate velocity  $v_p$  varies with plate length  $L$  for various choices of the fault zone and lithosphere strengths  $(\tau_f l_f)'$  and  $\eta'_l$ . Because value of the the mantle viscosity  $\eta_m$  is not well constrained, we use it as a free parameter that we can adjust to match the magnitude of plate velocities to those found on Earth.

The thickness of a plate as it begins to subduct depends on its age and hence on its length and velocity as in (4.11). This relationship between plate velocity and thickness is shown by solid lines in Figure 4.8 for plate lengths that correspond to those of the Cocos and Pacific plates ( $L = 1500$  and  $10,000 \text{ km}$ ). These curves are members of a larger family of curves that satisfy the thickness-age relationship of (4.11) for each value of  $L$ . To determine the velocity of plates of a given length, we apply (4.30). Curves for this expression are also plotted in Figure 4.8 for four models of  $\eta'_l$  and  $(\tau_f l_f)'$  and for the two values of  $L$ . The intersections of these two sets of curves are denoted by circles in Figure 4.8 and give the velocity and thickness of a plate for each of the four models and for the two plate lengths  $L$ . For each model of subduction zone strength we have chosen  $\eta_m$  in (4.30) such that the Cocos plate curves ( $L = 1500 \text{ km}$ , thin lines) intersect to give the actual Cocos plate velocity of  $8.6 \text{ cm yr}^{-1}$ . We then calculate, for each model, the velocity and thickness solutions for the Pacific plate ( $L = 10,000 \text{ km}$ , thick lines) using the same viscosity we used for the Cocos plate. We can evaluate each model of subduction zone strength by its ability to predict the Pacific plate velocity ( $8 \text{ cm yr}^{-1}$ ).

For a strong lithosphere, solutions only exist for the Pacific plate in the limit that the lithosphere grows very thick and velocities approach zero (observe that the thick curved solid line never crosses the dotted and dashed lines in Figure 4.8b). In fact,

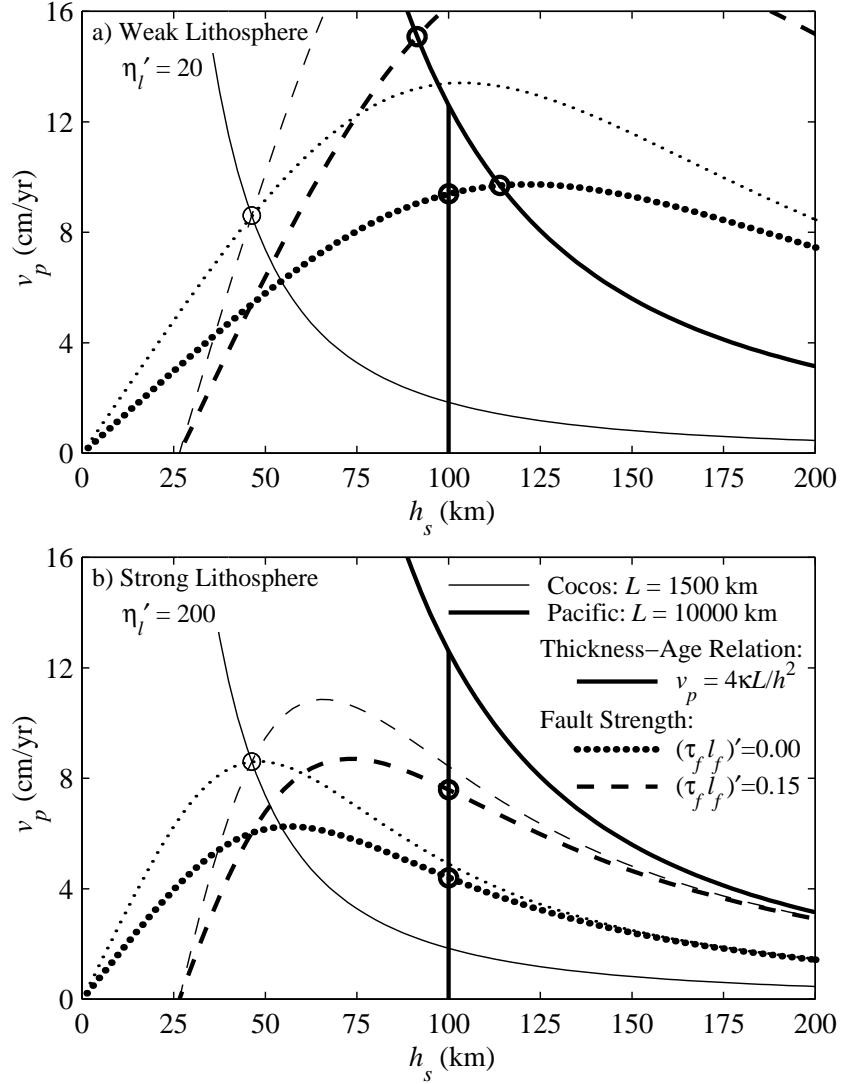


Figure 4.8: Solutions for the plate velocity  $v_p$  and thickness  $h_s$  of plates for two ridge-to-trench plate lengths  $L = 1500$  km for the Cocos plate (thin lines) and  $L = 10,000$  km for the Pacific plate (thick lines). Solid lines satisfy the thickness-age relationship (4.11). Dashed and dotted lines represent the balance between viscous dissipation and potential energy release given by (4.30). For cases in which the resulting plate thickness is larger than 100 km, we also plot the intersection of (4.30) and  $h_s = 100$  km, which represent solutions for plates that cannot grow thicker than 100 km. For each model of lithosphere and fault zone strength the mantle viscosity  $\eta_m$  is adjusted to yield the Cocos plate velocity of  $v_p = 8.6$  cm yr $^{-1}$  for  $L = 1500$  km. The required values of  $\eta_m$  can be estimated from Figure 4.11a. (a) Curves for a weak lithosphere of  $\eta'_l = 20$ . (b) Curves for a strong lithosphere of  $\eta'_l = 200$ . In both Figures 4.8a and 4.8b, the dotted and dashed lines show  $(\tau_f l_f)' = 0$  and 0.15 for a strong and weak fault zone, respectively.

if  $\eta'_l$  is large, both (4.30) and (4.11) have velocities that vary as  $1/h_s^2$  for large  $h_s$ , meaning that solutions only exist for  $v_p = 0$ . To obtain nonzero plate velocities and still allow strong plates, we must place a limit on the thickness of the lithosphere. This is perhaps not unrealistic because at some point a growing boundary layer must become unstable and cease to thicken [e.g., *Howard, 1964; Jaupart and Parsons, 1985*]. We thus disallow thickening beyond an age of 80 Ma, the point at which the linear relationship between seafloor depth and the square root of its age is observed to break down [e.g., *Parsons and Sclater, 1977*]. There is some controversy over whether this observation is real and over the physical mechanism by which it occurs if it is, but we will assume that this breakdown is accompanied by a corresponding cessation of plate thickening at 100 km, the thickness given by (4.11) for 80 Ma. Thus, if solutions to (4.11) and (4.30) require plate thickness  $> 100$  km, we allow solutions for both the thick plate and for  $h_s = 100$  km in Figure 4.8.

The four models of lithosphere and fault strength produce different variations of velocity with plate thickness, as shown by the dashed and dotted curves in Figure 4.8. If the fault zone is weak (dotted lines), the velocity variation with  $h_s$  depends on the two denominator terms of (4.30). For small  $h_s$  the bending term is small, so the constant mantle term dominates, causing (4.30) to increase approximately linearly with  $h_s$  as the buoyancy increases. As  $h_s$  increases, the lithosphere term begins to dominate, and the curve for (4.30) bends over and decreases as  $1/h_s^2$  for large  $h_s$ . The thickness at which the lithosphere term begins to become important depends on the dimensionless lithosphere viscosity  $\eta'_l$ . The effect of increasing the fault zone strength is to decrease the numerator of (4.30), causing zero velocity at a nonzero thickness and approximately shifting the curves for (4.30) to the right. As a result, the Pacific plate curves intersect the thickness-age relationship at different velocities for different combinations of fault zone and lithosphere strength (thick lines, Figure 4.8). Only two of the four models produce realistic plate velocities for both the Cocos and Pacific plates. If the lithosphere is weak (Figure 4.8a), the fault zone must also be weak (dotted line) or Pacific plate velocities are too large. If the lithosphere is strong (Figure 4.8b), nonzero plate velocities are only obtained if the maximum plate

thickness of  $h_s = 100$  km is enforced. In this case, realistic velocities of  $\sim 8$  cm yr<sup>-1</sup> are only obtained for the Pacific plate if the fault zone is also strong (dashed line).

The parameter space of dimensionless lithosphere and fault zone strength is more fully explored in Figure 4.9, where solutions for plate velocity are plotted as a function of plate length  $L$ . For each subduction model of lithosphere and fault zone strength, two solutions are given: one for which a maximum thickness of 100 km is enforced and one for which  $h_s > 100$  km is permitted. As before, the one remaining free parameter, the mantle viscosity  $\eta_m$ , is adjusted for each model so that plates of length  $L = 1500$  km have velocities equal to 8.6 cm yr<sup>-1</sup>, the set of values appropriate for the Cocos plate. We can now test a given model's validity by seeing if it gives realistic plate velocities for all values of  $L$  between the Cocos and Pacific plate lengths. It is clear that for all but the weakest lithosphere strengths, we must restrict the plate thickness to 100 km in order to get reasonable plate velocities at large  $L$ . For weak fault zones of  $(\tau_f l_f)' = 0.0$  (Figure 4.9a), a dimensionless lithosphere viscosity near  $\eta_l' = 60$  yields a variation of velocity with  $L$  that is confined to the observed range of 5 to 9 cm yr<sup>-1</sup>. Greater values of  $\eta_l'$  give velocities that are too small for large  $L$ , while smaller values yield velocities that are too large. As observed in Figure 4.8, larger fault zone strength requires greater dimensionless lithosphere viscosity. For example, if  $(\tau_f l_f)' = 0.15$  (Figure 4.9d), a lithosphere viscosity between about  $\eta_l' = 200$  and  $\eta_l' = 600$  seems to produce a good range of plate velocities. Intermediate fault zone strengths require intermediate dimensionless lithosphere strengths, as shown in Figures 4.9b and 4.9c. Thus we can obtain a reasonable set of plate velocities for all fault strengths  $(\tau_f l_f)'$  between 0.0 and 0.15 but only for specific values of the lithospheric strength  $\eta_l'$  that increase with fault strength.

The portion of the parameter space defined by the dimensionless lithosphere and fault zone strengths that yields Earth-like plate velocities for all plate lengths is highlighted in Figure 4.10. This region is defined such that all plates of lengths between 1500 and 10,000 km (representing the Cocos and Pacific plates) have velocities between 4 and 11 cm yr<sup>-1</sup>, a more liberal constraint than the one Earth places on the range of plate velocities. The band of models that produce acceptable plate velocities

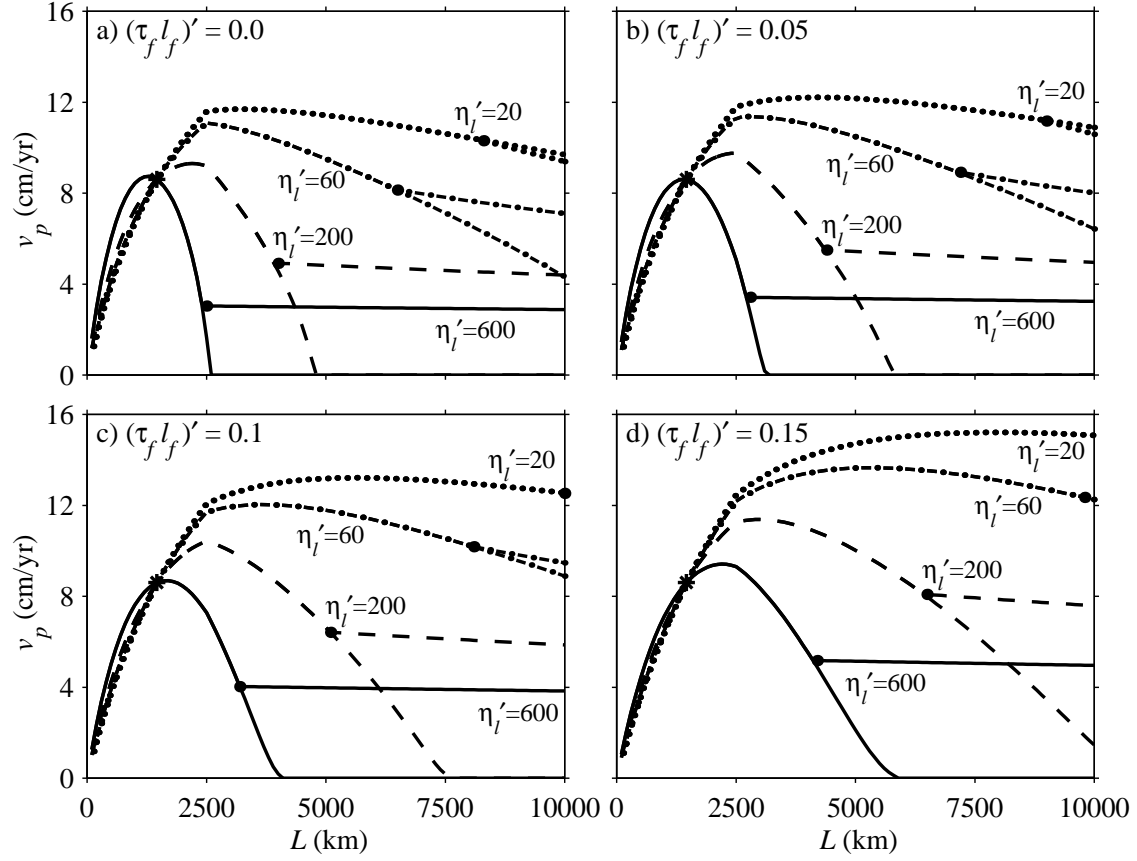


Figure 4.9: Plots of plate velocity  $v_p$  as a function of plate length  $L$  that represent solutions to (4.11) and (4.30) such as those shown in Figure 4.8. For each curve the mantle viscosity  $\eta_m$  is adjusted so that the curve gives a solution that fits the Cocos plate, where  $v_p = 8.6 \text{ cm yr}^{-1}$  and  $L = 1500 \text{ km}$  (denoted by a star). Two curves are given for each model, one in which a maximum plate thickness of 100 km is enforced and one in which it is not. The branching of the two models is denoted by a dot, with the smoother line representing the thick plate curve. Sixteen models are presented, showing fault strengths  $(\tau_f l_f)'$  of (a) 0.0, (b) 0.05, (c) 0.1, and (d) 0.15. Dotted, dash-dotted, dashed, and solid curves represent  $\eta_l'$  values of 20, 60, 200, and 600, respectively. The mantle viscosities associated with each model can be estimated from Figure 4.11a.

runs through values of  $(\tau_f l_f)'$  between 0.0 and about 0.2. As observed in Figure 4.9, strong fault zones for which  $(\tau_f l_f)' > 0.15$  require the lithosphere viscosity to be  $> 300$  times that of the mantle to produce reasonable plate velocities. For weaker fault zones, lithosphere viscosities between 50 and 300 times  $\eta_m$  are required.

The fraction of the total viscous dissipation that occurs in each region of the plate system is also shown in Figure 4.10, for plate lengths of 10,000 km (Pacific plate) and 1500 km (Cocos plate). For both the Pacific and Cocos plates the viscous dissipation in the lithosphere remains approximately constant throughout the shaded region. For the Pacific plate the lithosphere dissipates between 50 and 70% of the total potential energy (Figure 4.10c). This value is larger than the corresponding 15 to 30% for the Cocos plate (Figure 4.10f) because the Pacific plate bends into the mantle with the maximum thickness of  $h_s = 100$  km, which generates more dissipation. For the Cocos plate the decrease in lithosphere dissipation is accompanied by an increase in dissipation in both the fault zone and the mantle.

The correlation between the highlighted region of reasonable plate velocities and contours of lithosphere importance (Figures 4.10c and 4.10f) is a consequence of the two sharing the same pattern in dimensionless lithosphere-fault zone strength space. The fact that they do has a consequence for the dimensional value of lithosphere viscosity predicted by our models. The percentage of lithosphere dissipation is given by the ratio of (4.26) to (4.12). The result is proportional to  $v_p$ ,  $h_s^2$ ,  $\eta_l$ , and other parameters that are constant between models. Because the fraction of lithospheric dissipation is approximately constant in the region of reasonable velocities, the product of these three terms must be constant. We have defined  $v_p$  to be constant, and for large  $L$ ,  $h_s$  is a constant 100 km. Thus  $\eta_l$  should be constant among the acceptable models. This is shown in Figure 4.11b, in which the contours of dimensional lithosphere viscosity approximately follow the shaded region of realistic velocities. From Figure 4.11b, we estimate an effective viscosity for between about 60 and  $150 \times 10^{21}$  Pa s. Thus, as fault zone strength increases, the required increase in the dimensionless lithosphere viscosity  $\eta_l'$  is achieved through a decrease in mantle viscosity, not an increase in lithosphere viscosity.

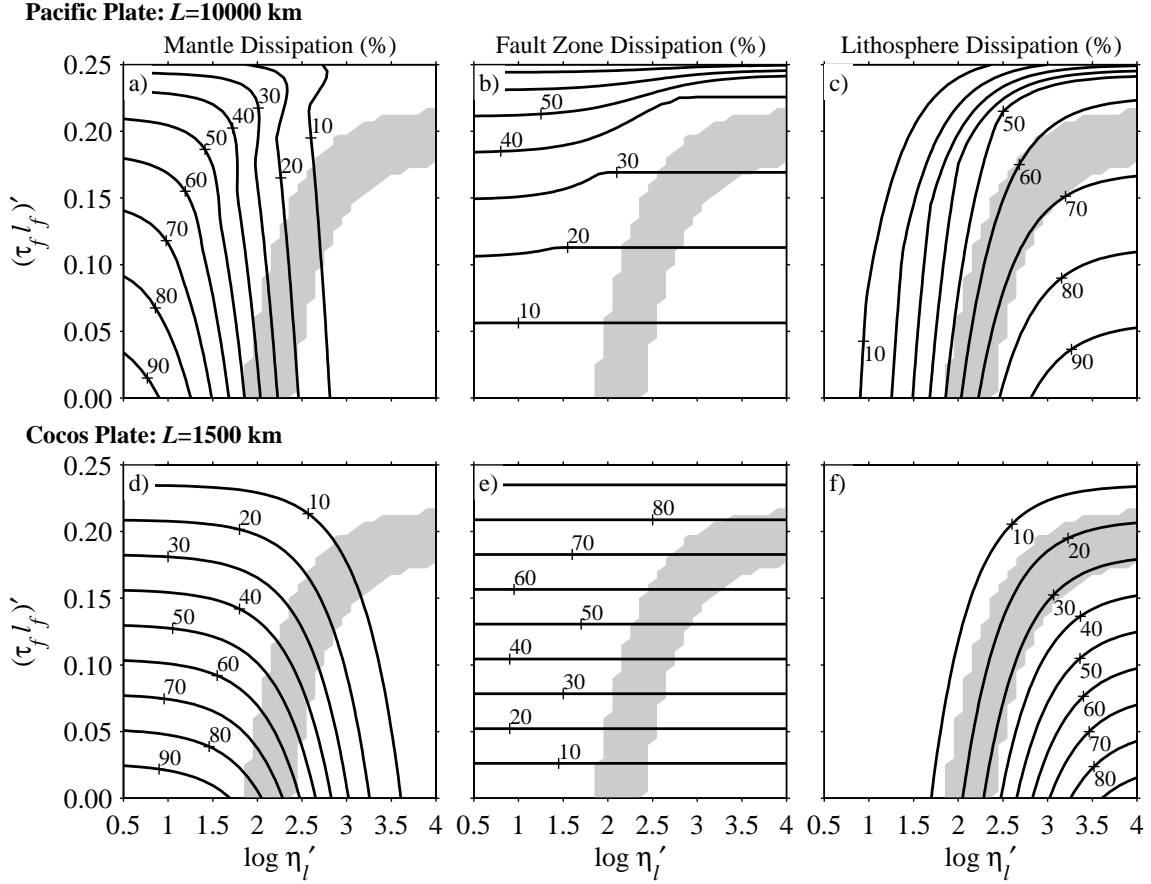


Figure 4.10: Model results that yield the Cocos plate velocity  $v_p = 8.6$  Pa s for the Cocos plate length  $L = 1500$  km for the solution of (4.11), (4.30), and  $h_s \leq 100$  km, plotted as a function of both lithosphere strength  $\eta_l'$  and fault zone strength  $(\tau_f l_f)'$ . The shaded region represents the portion of parameter space that produces a “realistic” distribution of plate velocities, defined such that plate velocities fall between 4 and 11 cm yr<sup>-1</sup> for all values of  $L$  between 1500 and 10000 km. To the upper left of the shaded region, maximum velocities are  $> 11$  cm yr<sup>-1</sup>; to its lower right, minimum velocities are  $< 4$  cm yr<sup>-1</sup>. The percentage of viscous dissipation that occurs in the (a) mantle, (b) fault zone, and (c) lithosphere are shown for a plate length of  $L = 10,000$  km, corresponding to the Pacific plate. (d), (e), and (f) show these percentages for a plate of length  $L = 1500$  km, corresponding to the Cocos plate.

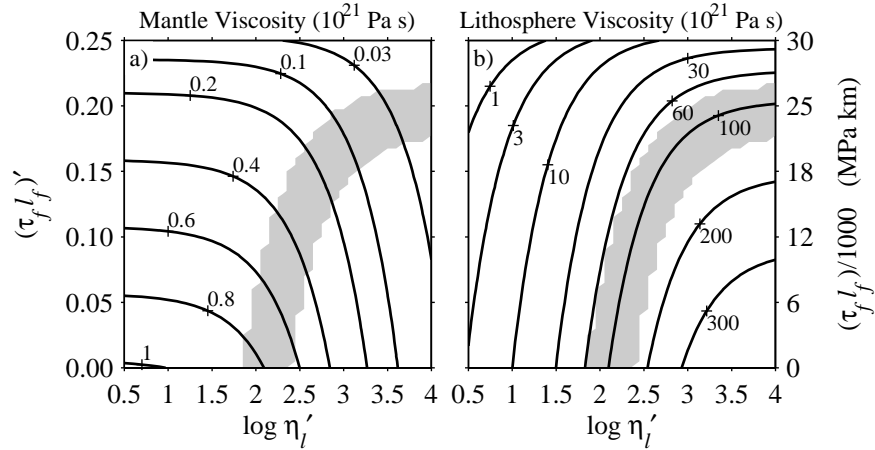


Figure 4.11: Results for the models shown in Figure 4.10, with the shaded area again representing the portion of parameter space that produces a realistic distribution of plate velocities. (a) Mantle viscosity, given in units of  $10^{21}$  Pa s, that is required to produce the Cocos plate velocity of  $v_p = 8.6$  cm/yr for the Cocos plate length,  $L = 1500$  km. (b) Lithosphere viscosity for these models, which is simply the product of the mantle viscosity and the dimensionless lithosphere viscosity (the horizontal axis). The vertical axis in Figure 4.11b is the same as that of Figure 4.11a, only expressed in dimensional units using (4.20) and the parameter values given in the text.

The results described above are obtained by adjusting one free parameter, the mantle viscosity, so that each model of lithosphere and fault zone strength yields the Cocos plate velocity of  $v_p = 8.6$  cm yr $^{-1}$  at  $L = 1500$  km length. Our results thus depend on our choice of the Cocos plate as a “reference” plate and may not be representative if the Cocos plate velocity is anomalously large or small. If it were greater than the observed value of 8.6 cm yr $^{-1}$ , the curves in Figure 4.9 should be shifted upward by a constant factor, making some of the large  $\eta'_l$  curves “realistic,” according to our previous definition. Similarly, if the Cocos plate velocity were decreased, curves for smaller values of  $\eta'_l$  would become appropriate. Indeed, tests show that the shaded regions in Figures 4.10 and 4.11 should be widened if we allow for a distribution of velocities for the Cocos plate. Similarly, the choice of another reference plate, such as the Nazca plate, serves to widen the range of “acceptable” subduction zone models. These changes, however, are not great, and we have already accounted for some of

this variation by using a liberal range of plate velocities to constrain our realistic set of subduction models. Thus we continue by drawing conclusions using the results shown in Figures 4.10 and 4.11 as a guide.

## 4.8 Application to the Earth's Subduction Zones

Independent estimates of mantle viscosity could be used in conjunction with Figure 4.11a to help constrain the strength of the lithosphere and fault zone. Estimates of mantle viscosity, however, are currently uncertain to within an order of magnitude, the range expressed in Figure 4.11a. In addition, because mantle viscosity varies significantly with depth, it is unclear how a mantle viscosity profile should be averaged in order to compare it to Figure 4.11a. In effect, we have defined the mantle viscosity in (4.8) as the viscosity that is needed to allow (4.8) to yield the total viscous dissipation in the mantle, which does not necessarily correspond to independent estimates derived from geoid or postglacial rebound studies. In addition, the viscosity estimates in Figure 4.11a are generated by assuming the effective length of the negatively buoyant portion of the slab to be  $l_s = 1000$  km. The value of this quantity is the subject of some controversy and may be diminished if the slab has difficulty penetrating the phase change [e.g., *Tackley, 1995*] or jump in viscosity [e.g., *Gurnis and Hager, 1988*] at 670 km depth. *Lithgow-Bertelloni and Richards [1995]*, on the other hand, estimate that slabs in the lower mantle contribute  $\sim 70\%$  of the total force needed to drive the plates, suggesting that  $l_s$  should extend deeply into the lower mantle. Our estimate of  $l_s = 1000$  km is intermediate between these two extremes, but if it is incorrect, the estimates of mantle and lithosphere viscosity (Figures 4.11a and 4.11b) should be changed in proportion to  $l_s$ , as shown by (4.30).

If the strengths of the lithosphere and the fault zones were well known, we could use Figure 4.10 to determine the relative importance of the mantle, lithosphere, and fault zone in dissipating convective energy. The effective lithosphere viscosity  $\eta_l$  is particularly difficult to constrain because it represents an attempt to relate the complicated rheological laws of non-Newtonian rheology and brittle failure to simple

viscous flow. In addition, any errors in our estimate of the radius of curvature of bending slabs,  $R$ , are mapped into  $\eta'_l$ . As shown by (4.30), an increase in  $R$  can be balanced by a corresponding increase in  $\eta'_l$  by the cube of the change in  $R$ . Thus it is difficult to precisely estimate  $\eta_l$  for Earth. Using  $R = 200$  km, the range of acceptable lithosphere viscosities is between 60 and  $150 \times 10^{21}$  Pa s (Figure 4.11b). The mantle viscosity required is close to  $10^{21}$  Pa s for weak fault zones and smaller for strong fault zones (Figure 4.11a). It is reasonable that significant temperature-dependent strengthening occurs in the lithosphere, so this range of lithosphere viscosities seems plausible.

To estimate the strength of the fault zone, we estimate its length and the shear stress it supports. An analysis of the seismicity under Japan [*Hasegawa et al.*, 1994] reveals low-angle thrust events occurring along the upper surface of the plate. If these earthquakes represent slip on the plate bounding fault, this fault appears to be  $\sim 200$  km long. The stress on such faults can be estimated in several ways. Earthquake stress drops on plate bounding faults are typically  $< 10$  MPa [e.g., *Hanks*, 1977; *Kanamori and Anderson*, 1975]. This provides a lower bound on the typical fault stress, but if earthquakes do not relieve all of the stress on the fault, the actual stress could be larger. *Hanks* [1977] speculates that plate-bounding faults support stresses of the order of 100 MPa down to  $\sim 15$  km, at which point the strength of rocks decreases due to an increase in temperature. *Hickman* [1991] suggests that although faults should be capable of supporting such stresses, the lack of heat flow anomalies associated with plate-bounding strike-slip faults indicates that the stress on these faults must be downward of 20 MPa. *Molnar and England* [1990], on the other hand, use heat flow estimates near major subduction zone thrust faults to estimate that stresses on these faults must exceed 30 MPa. Finally, *Zhong and Gurnis* [1994] show that trench topography is best matched in dynamic models of subduction zones if major thrust faults support shear stresses of 15 to 30 MPa to 100 km depth.

Average fault stresses of 10 to 100 MPa supported over 200 km yield fault strengths between 2000 and 20,000 MPa km, which, when made dimensionless using (4.20), yields  $(\tau_f l_f)'$  between about 0.017 and 0.17. This range gives essentially no constraint

on fault strength in Figures 4.10 and 4.11, but if we assume that faults are weak, we need only consider dimensionless fault strengths less than about  $(\tau_f l_f)' = 0.05$ . In this case, the dissipation in the fault zone must be  $< 10\%$  of the total for thick (Pacific) plates and  $< 20\%$  for thin (Cocos) plates (Figures 4.10b and 4.10e). Because the lithosphere dissipation is consistently  $\sim 60\%$  of the total for thick plates and  $20\%$  for thin plates (Figures 4.10c and 4.10f), the mantle component of dissipation is  $\sim 20 - 40\%$  for thick plates and  $60 - 80\%$  for thin plates (Figures 4.10a and 4.10d).

## 4.9 Discussion

To estimate the relative importance of the lithosphere, fault zone, and mantle in resisting convective motions, we use an energy balance between the rate of viscous dissipation and the rate of potential energy release. In doing so, we ignore the effects of heating associated with viscous dissipation in both our finite element calculations and our analytic theory. This is consistent with our assuming an incompressible fluid in (4.5), which eliminates the pressure work term. For a compressible fluid, including viscous dissipation mainly affects the details of the temperature field and hence the details of the distribution of internal buoyancy and potential energy release. *Backus* [1975] and *Hewitt et al.* [1975] show that for a compressible fluid the net cooling associated with the pressure term globally balances the temperature increase due to viscous heating. Thus we do not expect an important change in the global rate of potential energy release. Viscous heating might have an important effect locally in regions of concentrated dissipation such as fault zones and slabs because of the temperature dependence of effective viscosity. For fault zones, we already use an in situ effective rheology. For the slab although the rate of dissipation can be high, the time a parcel of material spends in a region of high dissipation is short, so its temperature increase is small.

By balancing viscous dissipation and potential energy release, we have defined a range of lithosphere and fault zone strengths for which plates move at speeds within the range observed on Earth ( $5 - 9 \text{ cm yr}^{-1}$ ). There are a few plates, however,

that do not move with velocities within this range. For one, the small Juan de Fuca plate is currently subducting at  $< 4 \text{ cm yr}^{-1}$  (Table 4.1). In fact, our model predicts a slow velocity for short plates (Figure 4.9) because the negative buoyancy of their thin subducted slabs is small. Another exception is the slow subduction of the North American, South American, and Antarctic plates under the Caribbean, Scotia, and South American plates [Jarrard, 1986]. The horizontal extent of these slabs represents only a small fraction of the perimeter of the plate to which they are attached [Forsyth and Uyeda, 1975], so we can not expect the pull of the subducted slab to be a significant driving force for these plates.

Plate velocities in the early Cenozoic (64-43 Ma) were slightly larger than those observed today. An examination of individual plate motions shows that the increase in plate velocity is significant for the Indian, Kula, and Farallon plates, which traveled close to  $14 \text{ cm yr}^{-1}$  in the early Cenozoic [Gordon and Jurdy, 1986]. Plate reconstructions [Gordon and Jurdy, 1986; Lithgow-Bertelloni and Richards, 1998] show that during this time period the Kula and Farallon plates were shrinking in size as their ridges moved closer to their subduction zones. Our model assumes that the plate is in a steady state. In particular, we assume that the plate thickness associated with buoyancy is the same as that associated with bending, so that the two values of  $h_s$  in the plate velocity equation (4.28) are the same. For a shrinking plate the slab is composed of material that subducted with an age older than that of the material that is currently subducting. Thus the thickness associated with buoyancy in the numerator of (4.28) should be larger than that associated with bending in the denominator. As a result, a shrinking plate should travel with a faster velocity than a plate that is in steady state. It is possible that the Kula and Farallon plates were propelled at faster rates during the early Cenozoic due to the fact that they were shrinking during this time period. The Indian plate, however, does not appear to change in size while its velocity is near  $14 \text{ cm yr}^{-1}$  [Gordon and Jurdy, 1986].

Other mechanisms could be responsible for variations in plate velocities. First, transform faults could affect a plate's velocity by forcing it to travel in a direction parallel to the fault's strike and at an angle to the pull of the subduction zone [e.g.,

*Lithgow-Bertelloni and Richards, 1998; Zhong et al., 1998*]. In addition,  $R$  or  $l_s$  could change with time or between plates, yielding variations in  $v_p$ , as shown in (4.28). Finally, complications to mantle convection induced by variations in viscosity and the presence of phase changes could affect plate motions [e.g., *Bunge et al., 1996; Hager and O'Connell, 1979; Tackley, 1995; Van der Hilst et al., 1997; Zhong and Gurnis, 1995a*].

We have shown, however, that the mantle plays an important role only for short plates and for long plates the lithosphere is dominant (Figure 4.10). Thus the mantle dynamics may play a secondary role to subduction zone dynamics in controlling the patterns and rates of mantle convection. This observation could have important implications for Earth's history and future. In an isoviscous Earth, plate velocities scale with mantle viscosity [e.g., *Turcotte and Oxburgh, 1967*]. Thus a small decrease in mantle temperature should cause plate velocities to slow considerably because mantle viscosity is highly temperature dependent. The strength of subduction zones, however, should primarily depend on Earth's surface temperature, which should remain fairly constant over most of Earth's history. If subduction zones indeed provide a primary resistance to convection in the mantle, the independence of their strength from changes in mantle temperature could cause plate velocities to be stabilized over geologic time, despite lower mantle viscosity during warmer periods of Earth's history. In the future, a cooling Earth should continue to convect in the current plate tectonic regime until mantle viscosity increases to the point at which it produces more dissipation than the bending lithosphere. From (4.28), we see that this requires about an order of magnitude increase in  $\eta_m$  unaccompanied by a similar change in  $\eta_l$ . Thus one role of strong subduction zones could be to stabilize plate tectonic rates over long periods of Earth's history.

Another parameter that is important in controlling plate velocities is the maximum thickness of the oceanic lithosphere, which we have taken here to be 100 km. If the lithosphere can grow thicker than this, the additional bending stresses, which depend on the cube of plate thickness, slow the plate considerably, causing the plate to cool and thicken even more. A Pacific-sized plate with no thickness restrictions

becomes frozen at zero plate velocity if its viscosity is  $\gtrsim 100$  times that of the mantle (Figure 4.9). This could throw the Earth into the rigid lid convective regime described by *Jaupart and Parsons* [1985] and *Solomatov* [1995]. It is interesting to speculate that the process that limits oceanic plate thicknesses on Earth, if it exists, could be the process that enables Earth to convect in a plate tectonic mode instead of a more Venus-like rigid lid mode. This process is likely to be affected by the temperature difference between the mantle and lithosphere and the temperature-dependent properties of the lithosphere, so it may depend on mantle temperature. If it does, a hotter mantle in the past, or a cooler one in the future, could change the maximum thickness of oceanic lithosphere and thus alter the plate tectonic style of Earth.

## 4.10 Conclusions

We have shown that the rheology of the lithosphere is crucially important in controlling the dynamics of convection in the mantle. The strength of fault zones and the effective viscosity of the lithosphere, which is probably affected by both brittle faulting and non-Newtonian viscous flow, are important quantities that control Earth's distribution of plate velocities. Thus, as anticipated by *Jaupart and Parsons* [1985] and *Solomatov* [1995], it is the strength of the upper boundary layer to convection in the mantle that determines the convective pattern of the mantle. We have found that for Earth it is how easily this upper boundary layer can bend and slide past neighboring lithosphere as it subducts that determines the mantle's convective style.

We have shown that at least 60% of the energy associated with the descent of a subducting slab attached to a long, thick plate is dissipated by the bending of the slab, and up to 10% more may be dissipated in the fault zone adjacent to the slab. For shorter, thinner plates, the bending contribution decreases. Because the subduction zone itself is so crucially important in determining the dynamics of plate tectonics and mantle convection on Earth, it is essential that subduction zones be handled carefully in numerical models of mantle convection. It is not clear that the implementation of convergent plate boundaries using piecewise continuous kinematic

boundary conditions, low-viscosity boundaries, or even a faulted lithosphere can accurately reproduce the extreme importance of the bending lithosphere in a numerical model. One solution may be to apply a complicated, high-resolution gridding scheme, like the one used here in a local study, to a global mantle flow calculation. This would require intense gridding and computational effort. Alternatively, a more sophisticated parameterization of subduction zones must be developed that mimics the dissipation patterns of bending and fault zone shear that occur in real subduction zones.

**Acknowledgments.** This work was supported in part by National Science Foundation grant 9506427-EAR, NASA grant NAG5-6352, and by a National Science Foundation Graduate Research Fellowship. We thank M. Gurnis, P. Molnar, R. O'Connell, and S. Zhong for discussions and comments that improved the manuscript, and M. Riedel and B. Schott for helpful reviews.

